3s Rydberg and Cationic States of Pyrazine Studied by Photoelectron Spectroscopy

Mizuki Oku[†]

Department of Basic Science, Graduate School of Arts and Sciences, The University of Tokyo, Tokyo 153-8902, Japan

Yu Hou, Xi Xing, Beth Reed, Hong Xu, Chao Chang, and Cheuk-Yiu Ng

Department of Chemistry, University of California at Davis, Davis, California 95616

Kiyoshi Nishizawa, Keijiro Ohshimo, and Toshinori Suzuki*

Chemical Dynamics Laboratory, RIKEN, Wako 351-0198 Japan

Received: September 5, 2007; In Final Form: October 19, 2007

We have studied 3s(n^{-1} and π^{-1}) Rydberg states and $D_0(n^{-1})$ and $D_1(\pi^{-1})$ cationic states of pyrazine [1,4-diazabenzene] by picosecond (2 + 1) resonance-enhanced multiphoton ionization (REMPI), (2 + 1) REMPI photoelectron imaging, He(I) ultraviolet photoelectron spectroscopy (UPS), and vacuum ultraviolet pulsed field ionization photoelectron spectroscopy (VUV−PFI-PE). The new He(I) photoelectron spectrum of pyrazine in a supersonic jet revealed a considerably finer vibrational structure than a previous photoelectron spectrum of pyrazine vapor. We performed Franck−Condon analysis on the observed photoelectron and REMPI spectra in combination with ab initio density functional theory and molecular orbital calculations to determine the equilibrium geometries in the D_0 and 3s(n^{-1}) states. The equilibrium geometries were found to differ slightly between the D_0 and 3s states, indicating the influence of a Rydberg electron on the molecular structure. The locations of the D_1-D_0 and 3s(π^{-1})−3s(n^{-1}) conical intersections were estimated. From the line width in the $D_1 \leftarrow S_0$ spectrum, we estimated the lifetime of D_1 to be 12 fs for pyrazine and 15 fs for fully deuterated pyrazine. A similar lifetime was estimated for the 3s(π^{-1}) state of pyrazine by REMPI spectroscopy. The vibrational feature of D_1 observed in the VUV−PFI-PE measurement differed dramatically from that in the UPS spectrum, which suggests that the high-*n* Rydberg (ZEKE) states converging to the D_1 vibronic state are short-lived due to electronic autoionization to the D_0 continuum.

I. Introduction

Time-resolved photoelectron imaging (TRPEI) is a powerful experimental technique to study ultrafast excited-state dynamics.[1] In our first femtosecond TRPEI study,[2] we applied (1 + 2′) two-color resonance enhanced multiphoton ionization (REMPI) to the S_1-T_1 intersystem crossing (ISC) in pyrazine that is the best-known example of an intermediate coupling case in molecular radiationless transition.[3−15] The pump pulse of 324 nm was resonant with the 0_0^0 band of the $S_1 \leftarrow S_0$ transition, and the probe pulse of 400 nm induced two-photon ionization via resonance with the quasicontinuum of highly excited vibrational states in the 3s(n^{-1}) Rydberg state at the energy of $\hbar\omega_{pump} + \hbar\omega_{probe}$.[2] When the probe pulse was time-delayed more than 100 ps after the pump pulse, two-photon ionization from the T_1 state, populated by ISC from S_1, started to appear via resonance with the vibrational quasicontinuum in the triplet 3s(n^{-1}) state. We performed detailed measurements of time-dependent photoelectron speed and angular distributions and their theoretical analysis to understand rotational wavepacket motions in the bright (S_1) and dark (T_1) states and the ISC dynamics.[16−18] A similar (1 + 1′) REMPI measurement of pyrazine was also carried out,[19] which agreed well with the (1 + 2′) REMPI measurement.[16−18]

In addition to the experiments on the S_1-T_1 ISC of pyrazine, Song, Tsubouchi, and Suzuki (STS) investigated the nature of the 3s and 3p Rydberg states that were used as the second resonance states in (1 + 2) REMPI from S_1.[20] STS employed two-color (1 + 2′) and one-color (2 + 1) REMPI schemes using femtosecond lasers to observe the 3s(n^{-1}), 3p(n^{-1}), and 3s(π^{-1}) states. Previously, (2 + 1) REMPI of pyrazine via the 3s(n^{-1}) Rydberg state has been reported by Turner et al.[21] and Dion and Bernstein[22] with nanosecond lasers. STS found that the femtosecond REMPI differs markedly from the nanosecond REMPI in that the former was free from concomitant (1 + 2) REMPI via T_1 that had been strongly observed in the latter.[21] The difference is ascribed to a short lifetime (ca. 300 fs[22]) of the 3s Rydberg state, as it suppresses the efficiency of (2 + 1) REMPI via the 3s state to a comparable level in intensity with the (1 + 2) REMPI via T_1, when nanosecond lasers are employed. On the other hand, the drawback of a spectrally broad femtosecond laser was that it did not allow observation of fine vibrational structures in the REMPI spectrum.[20]

In the present work, we revisit (2 + 1) REMPI of pyrazine with a picosecond laser to perform detailed Franck−Condon analysis and examine the molecular structure in the 3s Rydberg state. The structure in the 3s state should be compared with that in D_0; however, the He(I) photoelectron spectrum of pyrazine vapor in the literature[23,24] offers neither sufficient resolution nor spectral accuracy for close comparison with a

* To whom correspondence should be addressed. E-mail: toshisuzuki@riken.jp.

† Junior Research Associate at RIKEN.

10.1021/jp0771466 CCC: $40.75
Published on Web 02/23/2008

high-resolution (2 + 1) REMPI spectrum. Therefore, we employ a new He(I) UPS apparatus with a supersonic molecular beam constructed in our laboratory. Comparison of the (2 + 1) REMPI and He(I) photoelectron spectra reveals an influence of the Rydberg electron on the structure of the ion core. Another important new piece of information obtainable from the new He(I) spectrum is the internal conversion dynamics from $D_1(\pi^{-1})$ to $D_0(n^{-1})$. It is known that $D_1(\pi^{-1})$ and $D_0(n^{-1})$ potential energy surfaces undergo a conical intersection (CI),[25] similarly with the case of $S_2(\pi\pi^*)$ and $S_1(n\pi^*)$ of pyrazine.[26−32] This also raises an interesting question about pulsed field ionization photoelectron (PFI-PE) spectroscopy of pyrazine.

The PFI-PE method provides the ultimate spectral resolution in photoelectron spectroscopy.[33−39] The PFI-PE measurement utilizes long-lived Rydberg states, so-called ZEKE states, below the individual rovibronic ionization thresholds for observation of the (action) spectrum. An interesting issue in the PFI-PE study of pyrazine is that the D_1 state of pyrazine seems to undergo rapid internal conversion down to D_0, which may affect the PFI-PE signal. Although Johnson and co-workers have previously reported a (1 + 1′) PFI-PE spectroscopic study of pyrazine via the $S_1(n\pi^*)$ state,[40] the present study is different from their work in that we employ one-photon ionization of pyrazine from S_0 by VUV laser.

From the (2 + 1) REMPI spectrum via the 3s Rydberg state and the He(I) UPS spectrum, we can determine the difference in molecular geometry between the 3s and D_0 states. This difference can also be examined independently by observing a photoelectron spectrum from the 3s Rydberg state. When the molecular structure of the Rydberg state is the same as that in the cationic state, a propensity rule of $\Delta v = 0$ holds (v represents vibrational quantum numbers) upon ionization. Thus, we employ (2 + 1) REMPI photoelectron imaging to examine the geometrical change between the 3s and D_0 states. Thus, all of the three transitions among S_0, 3s, and D_0 are examined using three different experimental methods.

II. Experimental Section

A. Picosecond (2 + 1) REMPI Spectroscopy and Photoelectron Imaging at RIKEN. A sample gas, 1% pyrazine in N_2, was continuously expanded into a vacuum chamber with a stagnation pressure of 760 Torr through a nozzle with an orifice 50 μm in diameter. The source chamber was pumped by a 1400 L/s turbo molecular pump (Pfeiffer, TMU1601P) backed by a scroll pump (Edward, ESDP30) with a liquid-nitrogen trap in the fore line. The supersonic jet was collimated by a conical skimmer with an orifice diameter of 2 mm located 50 mm downstream from the nozzle. The molecular beam was then introduced into an ionization chamber, where the background pressure was kept at about 1×10^{-7} Torr by a 500 L/s turbo molecular pump (SEIKO, STP-451C2Ω).

The 80 MHz, 300 mW output of a diode-pumped mode-locked Ti:sapphire laser (Coherent, Vitesse) was amplified by a hybrid regenerative/linear amplifier (Quantronix, Titan) pumped by a 500-Hz Nd:YLF (Quantronix, model 527) laser to generate a pulse train of ∼3.6 mJ/pulse, centered at 800 nm. The pulse width was measured to be 2.8 ps from the autocorrelation. A 60% of the output beam from the amplifier was frequency-doubled in a BBO crystal, and the resulting second harmonic was used to excite an optical parametric amplifier (OPA) that generates a tunable UV light ∼40 μJ/pulse in 330−395 nm with a bandwidth of ∼20 cm^{-1}. The UV beam was focused with a concave mirror ($f = 500$ mm) on the molecular beam at 165 mm downstream from the nozzle.

Pyrazine in the molecular beam was ionized by (2 + 1) REMPI, and photoelectrons thus generated were accelerated in a static electric field with the velocity mapping electrodes of Wrede et al.[41] Both the acceleration and field-free regions (780 mm) were shielded by a μ-metal tube to prevent the influence of the terrestrial magnetic field. At the end of the flight tube, electrons were detected by a microchannel plate (MCP: Galileo, $\phi = 40$ mm). The photoelectron current signal from the MCP was amplified by a preamplifier (NF Corp., SA230F5). In measurements of TRPEI, electrons were detected by an MCP backed by a phosphor screen (Hamamatsu F2226−24 PGFXR, $\phi = 70$ mm). Transient images on the phosphor screen were recorded by a thermoelectrically cooled charge-coupled-device (CCD) camera (Princeton Instruments, 512 × 512 pixel and 16 bits or Andor, 1024 × 1024 pixel and 32 bits).

Since the REMPI efficiency strongly depends on the laser intensity, we carefully stabilized the intensity with a variable neutral density filter while scanning the laser wavelength. In addition, for minimizing the influence of the fluctuation of laser pulse energy on the REMPI spectrum, we monitored the laser intensity with a joulemeter (Molectron, J3-09) on the shot-to-shot basis and registered the REMPI signal only when the observed pulse energy was within 36∼38 μJ/pulse. The absolute wavelength of the laser was calibrated using a monochromator (SPEX, 1704: resolution 0.006 nm) at various wavelengths, and the relative laser wavelength in scanning of the OPA was monitored from the Etalon fringes. The photoelectron signal, the UV intensity, and the Etalon fringe signal were simultaneously measured by gated boxcar integrators (SRS, SR250) and a personal computer.

The linewidths in the $3s(n^{-1}) \leftarrow\leftarrow S_0$ transition were examined using a nanosecond laser. The third harmonic of the output of a 10-Hz Nd:YAG laser (Spectra Physics, GCR170-10) was used to pump a dye laser (Lumonics HD-500B: Exalite 392A and 411 dyes in dioxane). The output pulse of the UV light from the dye laser was focused onto the molecular beam with a lens with $f = 600$ mm. In nanosecond REMPI experiments, the sample gas was expanded into the vacuum through a piezo-electric pulsed nozzle synchronized with the laser.

B. He(I) Ultraviolet Photoelectron Spectroscopy in Supersonic Jet at RIKEN. We have constructed a new apparatus for He(I) UPS combined with liquid beams and supersonic molecular beams. The apparatus consists of a molecular beam source, an ionization chamber, a beam dumper, a He discharge light source and a hemispherical electron energy analyzer (Gammadata Scienta, SES100, $R = 100$ mm). The ionization chamber made of stainless steel accommodates an inner wall made of μ-metal to suppress the terrestrial magnetic field penetrating from the vacuum ports. In this study, we removed a bulkhead separating the beam source and the ionization chamber to employ unskimmed supersonic jets. Prior to installation of a stainless-steel gas nozzle inside the μ-metal shield of the ionization chamber, a residual magnetic field on the nozzle was erased thoroughly with a demagnetizer (KANETEC). After installation of the nozzle, a stray magnetic field at the ionization point was measured to be less than 200 nT with a fluxgate magnetometer (Bartington, Mag-01H and Probe B). Without the bulkhead, both chambers were pumped together by two turbo molecular pumps (Osaka vacuum, TG2000MCA, 2000 L/s) backed by a scroll pump (Edwards, ESDP30B) through a liquid-nitrogen trap in the fore line.

An electron cyclotron resonance He-discharge lamp and a monochromator (Gammadata, VUV5000 and VUV5040) provided unpolarized He(I) emission (21.218 eV, a line width of

~1.2 meV) with a photon flux over 5×10^{12} photons/s (the manufacturer's specification) in the ionization volume of 3 mm ϕ. The molecules in the supersonic jet were ionized at ca. 20 mm downstream from the nozzle, and emitted photoelectrons were sampled by an electron lens system whose axis was perpendicular to both propagation directions of He(I) light and the supersonic jet. The lens system transferred photoelectrons to a curved entrance slit (0.4 mm in width, 14 mm in length) for a hemispherical electron-energy analyzer. The voltages applied to the electron lens system and the hemispherical analyzer were controlled by a personal computer. The spectra were measured by changing acceleration/deceleration voltages applied to the electron lens while maintaining a constant energy band-pass in the hemispherical analyzer. The energy-dispersed electrons through the analyzer were detected with a multichannel detector with Chevron MCPs (Hamamatsu, F1225-09) backed by a phosphor screen and a CCD camera (BASLER, A312f). Image acquisition and processing to convert observed images to photoelectron spectra were performed on the computer. The best photoelectron energy resolution of the apparatus was evaluated to be 2.9 meV (fwhm) at 5.459 eV based on the line width of the $Ar^+(^2P_{3/2})$ photoelectron band observed in the photoelectron spectrum of Ar in a supersonic beam.

A buffer chamber, pumped by two turbo molecular pumps (Leybold, TURBOVAC, 50L/s), separated the ionization chamber and the electron lens system. Apertures with holes of 5 and 10 mm ϕ could be mounted on both sides of the buffer chamber to minimize the conductance though the buffer. However, since these grounded apertures seemed to disturb the electric fields of the electron lenses and degrade the spectral resolution, they were dismounted for high-resolution measurements. The electron lens section was pumped by a turbo molecular pump (Osaka vacuum, TG220FCAB, 220L/s) through 408 holes (3 mmϕ) on the μ-metal shield covering the lenses. The hemispherical analyzer section was pumped by a turbo molecular pump (Osaka vacuum, TG220FCAB, 220L/s). The entrance slit of the analyzer and a rectangular hole (8 mm × 15 mm) in the middle of the electron lens section restricted the gas conductance, achieving 4-stage differential pumping as a whole. The pressures of the ionization chamber and the analyzer could be kept below 1×10^{-5} and 2×10^{-6} Torr, respectively, while running a CW supersonic jet.

The pyrazine (15%) seeded in helium was continuously expanded into the vacuum chamber through a pinhole 50 μm in diameter at a stagnation pressure of 110 Torr. Helium was used as a carrier gas as it is not ionized by He(I) light. The absolute photoelectron energy gradually drifted over time, which is perhaps due to variation of a work function with adsorption of sample molecules on the metal surface of the apparatus. Therefore, we introduced a trace amount of N_2 in a carrier gas and calibrated the absolute photoelectron kinetic energy by measuring $X^2\Sigma_g^+ - X^1\Sigma_g^+$ $v' = 0 \leftarrow v'' = 0$ photoelectron band of N_2.[42] Both of the photoelectron spectra of pyrazine and N_2 were measured in each scan. A single scan of the entire spectrum took about 5 min, and 280 sweeps were integrated to improve the S/N ratio. We used a three-point median filter to remove dark counts of the MCP in an individual sweep. The spectral resolution of the integrated photoelectron spectra of pyrazine was 5.5 meV.

C. VUV−PFI-PE Spectroscopy at UC Davis. The experimental arrangement and procedures for the VUV−PFI-PE measurement have been described in detail.[38] Briefly, the VUV laser radiation was generated by nonlinear four-wave frequency mixing in a Kr jet. The UV frequency ω_1 was fixed at 212.556 nm (202.316 nm) to match the two-photon resonance of the 5p ← 4p (5p′ ← 4p) transition. The visible laser output ω_2 was tuned to generate the desired VUV laser frequency range based on the difference-frequency mixing scheme ($2\omega_1 - \omega_2$). The ω_1 and ω_2 frequencies were generated by two dye lasers, which were pumped by an identical Nd:YAG laser (model PRO-290, Quanta Ray, Spectra Physics) operated at 15 or 30 Hz. In this experiment, the Kr gas jet assembly was housed in a nonlinear mixing chamber, which was evacuated by a 100 or 500 L/s turbomolecular pump. A pulsed valve (general valve, repetition rate = 30 Hz) was connected to the middle entrance of a T-shape channel (diameter = 1 mm), such that Kr from the pulsed valve entered the middle of the T-shape channel and exit symmetrically through the opposite ends of the perpendicular section of the channel. The axis of this section, which defines a 30 mm long gas channel, was aligned along the propagating axis of the UV and visible laser beams. The temporally compensated ω_1 and ω_2 laser beams were merged by a dichroic mirror before entering the nonlinear mixing chamber through a fused silica window to pass through the Kr gas channel, where the VUV radiation was generated. The VUV radiation of interest resulting from the four-wave difference-frequency mixing was selected by a windowless monochromator before entering the photoionization region. The VUV intensities emerging from the monochromator were monitored by a Cu photoelectric detector.

The pyrazine sample (2% seeded in Ar) was introduced into the photoionization region through a pulsed valve (general valve, nozzle diameter = 0.5 mm, stagnation pressure = 760 Torr) operated at 15 or 30 Hz to synchronize with the VUV laser beam. The supersonic jet of pyrazine thus generated was skimmed by a conical skimmer (ϕ = 1 mm) prior to intersecting the VUV laser beam at the photoionization region. The beam source chamber and photoionization chamber were evacuated by a 10 in. water-cooled diffusion pump (5000 L/s) and a turbo molecular pump (600 L/s) and were maintained at pressures of 10^{-5} and 10^{-7} Torr, respectively, during the experiment.

A dc field of <0.2 V/cm was applied to the photoionization region for sweeping the prompt background electrons away from the MCP detector. After a delay of 1−3 μs with respect to the firing of the VUV laser, a PFI field of 0.3 V/cm (width = 100 ns) was applied to the photoionization region to induce field ionization of high-n Rydberg molecules prepared by VUV excitation. This PFI field also served to extract PFI-PEs toward the MCP detector. The PFI-PE and VUV signals from the respective MCP detector and the Cu photoelectric detector were fed into independent boxcar integrators (SRS, SR250), which were interfaced to a personal computer. The computer also controlled the scanning of the dye lasers and the synchronization of the VUV laser beam and the pyrazine molecular beam. The Stark shift for PFI-PE measurements associated with our apparatus has been shown to be governed by the relation $4.1\sqrt{F}$ cm^{-1}, where F is the PFI pulse in V/cm.

III. Quantum Chemical Calculations

We have performed density functional theory (DFT) and molecular orbital (MO) calculations for the neutral ground state and the cationic ground state (D_0) of pyrazine. Equilibrium geometry optimizations and harmonic vibrational frequency calculations were carried out at the spin-unrestricted B3LYP/cc-pVTZ level using Gaussian 03[43] and the spin-restricted CCSD(T)/cc-pVTZ level using MOLPRO.[44] At the former level, anharmonic correction was made on the frequencies. Although pyrazine is in the D_{2h} symmetry in S_0,[45] Zhu and Johnson have

TABLE 1: Equilibrium Geometry of Pyrazine in the Neutral and Cationic Ground States

	S_0			D_0		
	expt.[a]	B3LYP cc-pVTZ[b]	CCSD(T) cc-pVTZ	B3LYP cc-pVTZ	CCSD(T) cc-pVTZ	FC analysis
NC/Å	1.3376	1.3321	1.3403	1.3000	1.3092	1.309(2)
CC/Å	1.3968	1.3906	1.3970	1.4269	1.4334	1.424(5)
CH/Å	1.0831	1.0838	1.0839	1.0842	1.0844	1.088(1)
CNC/°	115.65	116.06	115.14	125.03	124.49	124.7(2)
NCC/°	122.18	121.97	122.43	117.49	117.76	117.7(2)
HCN/°	117.87	117.19	116.97	121.82	121.67	121.4(5)

[a] r_α structure determined by electron diffraction and liquid crystal NMR [ref 46]. [b] Our calculations are in agreement with Martin and van Alsenoy.[48]

suggested that the geometry of pyrazine in D_0 may relax from D_{2h} symmetry.[40] In order to examine this possibility, we performed geometry optimizations starting from a chair and a boat form of pyrazine, which, however, resulted in the same planar optimum geometry. Thus, we conclude that pyrazine has D_{2h} symmetry in D_0. The equilibrium geometries, i.e., bond distances (r) and bond angles ($\angle$), calculated for S_0 and D_0 are summarized in Table 1 along with the experimental values obtained by an electron diffraction (ED) study.[46] An earlier ED study by Bormans et al.[47] reported r(C−N) = 1.339 Å and r(C−C) = 1.403 Å, whereas these values were refined to be r(C−N) = 1.3376 Å and r(C−C) = 1.3968 Å by Cradock et al.[46] The geometry calculated for S_0 at the B3LYP/cc-pVTZ level is in good agreement with the experimental results. The largest differences between calculated and experimental values are only 0.0062 Å in bond lengths and 0.68° in bond angles. It has been shown that the B3LYP/cc-pVTZ level calculations well reproduce the experimentally determined equilibrium structures of other azabenzenes.[48] Calculated values at the CCSD(T)/cc-pVTZ level for S_0 also agree with the experimental values, although the calculated HCN angle is slightly smaller by 0.9° than the experimental value. Both of the DFT and MO calculations suggest a significant change of the equilibrium geometry between S_0 and the D_0. The r(C−N) in D_0 is shorter than that in S_0, whereas the r(C−C) is longer in D_0. The $\angle$(CNC) and $\angle$(HCN) are larger, and the $\angle$(NCC) is smaller in D_0. The change of r(C−H) is negligible.

Table 2 lists the calculated and experimental vibrational frequencies[21,40,49,50] in S_0, D_0, and 3s(n^{-1}) of pyrazine (pyrazine-H4). Our values are closer to the experimental results than the calculations by Martin and van Alsenoy,[48] since we made anharmonic correction. We followed the vibrational mode numbering by Mulliken.[51] The calculated anharmonic frequencies at the B3LYP/cc-pVTZ level for the neutral ground state agreed with the experimental values within 5%. The vibrational frequency of the mode 10a calculated for D_0 at the CCSD(T)/cc-pVTZ level is unrealistically high, so the vibrational frequencies for D_0 obtained at this level are only for qualitative reference in this work. The calculated frequencies at the CCSD(T)/cc-pVTZ level for the neutral ground state are slightly larger than the experimental values, because anharmonic correction was not included at this level. Table 3 summarizes the calculated and experimental vibrational frequencies of deuterated pyrazine (pyrazine-D4).[52]

IV. Results

A. Picosecond (2 + 1) REMPI Spectrum of Rydberg States. Figure 1 shows the entire (2 + 1) REMPI spectrum of pyrazine-H4 observed via the 3s(n^{-1} and π^{-1}) Rydberg states. The 3s(n^{-1}) ← ← S_0 and 3s(π^{-1}) ← ← S_0 bands appear around the ranges of 50 000−56 000 and 56 000−60 000 cm^{-1}, respectively. The three spectra were obtained with (a) femtosecond,[20] (b) picosecond, and (c) nanosecond laser.[21] The femtosecond REMPI spectrum adapted from ref 20 is not corrected for the laser intensity variation over the wavelength, so it is shown here only for comparison of the resolution with those of the picosecond and nanosecond spectra. Comparison of panels a and b in Figure 1 reveals considerable improvement of spectral resolution in picosecond REMPI than that in femtosecond REMPI. Spectral broadness in femtosecond REMPI is presumably due to both the laser bandwidth and power broadening. The bands indicated by asterisk in nanosecond REMPI [Figure 1c] are due to the (1 + 2) REMPI signal via T_1, which are missing in picosecond REMPI [Figure 1b] and femtosecond REMPI [Figure 1a]. As explained in the introduction, the appearance of these bands via T_1 indicates the inefficiency of (2 + 1) REMPI via 3s states with a nanosecond laser. From the picosecond REMPI spectrum, we determined the term value of the 3s(n^{-1}) of pyrazine-H4 to be 50 844(8) cm^{-1}, which is in fair agreement with the literature values, 50 830(13) cm^{-1} by Turner et al.[21] and 50 835 cm^{-1} by Bernstein et al.[22] both by nanosecond (2 + 1) REMPI, 50 880 cm^{-1} by VUV absorption spectroscopy,[53] and 50 700 cm^{-1} by the femtosecond (1 + 2′) photoelectron imaging.[20] Similarly, the term value of 3s(π^{-1}) was determined to be 57 505(8) cm^{-1} in this work. With these refined terms values, the quantum defects of the 3s(n^{-1}) and 3s(π^{-1}) of pyrazine-H4 are calculated to be 0.865 and 0.884, respectively. We also determined the 3s(n^{-1}) origin band of pyrazine-D4 to be 50 997(8) cm^{-1} and the 3s(π^{-1}) origin band of D4 to be 57 452(14) cm^{-1}.

In the picosecond REMPI spectrum of Figure 1b, long vibrational progressions are observed in the region of 3s(n^{-1}), suggesting that the geometry of 3s(n^{-1}) differs considerably from that in S_0. On the other hand, since vibrational progressions are short in the 3s(π^{-1}) region, the equilibrium geometry in this state is similar to that in the neutral ground state. As seen later, the ratio for the intensity of 3s(π^{-1}) over that of 3s(n^{-1}) in picosecond REMPI is smaller than that for the intensity of D_1(π^{-1}) over that of D_0(n^{-1}) in He(I) UPS. The weakness of 3s(π^{-1}) in picosecond REMPI is due, at least in part, to a shorter lifetime of 3s(π^{-1}) than that of 3s(n^{-1}). Indeed, the observed line width of the origin band of the 3s(π^{-1}) ← ← S_0 of pyrazine-H4 was as large as 390 cm^{-1} (corresponding to the lifetime of ∼14 fs), which is an order of magnitude greater than that of the origin band of 3s(n^{-1}) ← ← S_0. For pyrazine-D4, the observed line width of the 3s(π^{-1}) origin band was 370 cm^{-1}.

The fwhm of the origin band of 3s(n^{-1}) ← ← S_0 of pyrazine-H4 measured with a picosecond laser increased for a higher laser power, hinting a power broadening effect. In order to ascertain this effect, we examined (3 + 1) REMPI of Xe via the 5p5d[3/2]$_1$ state[54] using various focusing conditions and laser powers. The line width was found to vary from 20 to 40 cm^{-1} depending on the photon density, which confirmed the power broadening effect at the laser intensity that we employed. In fact, the narrowest line width, 37 cm^{-1}, obtained by picosecond (2 + 1) REMPI of pyrazine was still larger than the value of 15 cm^{-1} previously reported by nanosecond (2 + 1) REMPI.[22] Thus, we reproduced the nanosecond REMPI of pyrazine-H4 and confirmed that the line width of the 0_0^0 band is 15(2) cm^{-1} when it is fit by a Lorentzian function. A similar measurement for (2 + 1) REMPI via the $6a^1$ level yielded 17-(1) cm^{-1}, which is slightly larger than that of the 0_0^0 band as shown in Figure 2.

TABLE 2: Comparison of Experimental and Theoretical Vibrational Frequencies (cm^{-1}) of Pyrazine-H4 in the S_0, D_0, and $3s(n^{-1})$ Rydberg States

		S_0			D_0					3s Rydberg		
vibrational mode		B3LYP	CCSD(T)	Innes[a]	B3LYP	CCSD(T)	ZEKE[b]	this work He(I) UPS	this work VUV -PFI-PE	Turner[c]	Goto[d]	this work REMPI
a_g	2	3028	3194	3055	3048	3209			3050.6(10)			
	8a	1571	1623	1582	1439	1479	1580	1417(8)	1418.4(10)	1435	1433	1472(9)
	9a	1237	1250	1230	1192	1206	1180	1187(8)	1193.9(10)		1171	1085(4)
	1	1025	1026	1015	1014	1021	1004	1010(8)	1004.8(10)	989		1010(9)
	6a	604	601	596	632	647	632	635(8)	635.8(10)	624	630	639(3)
a_u	17a	991	992	960	943	943						
	16a	343	349	341	393	409	384					
b_{1g}	10a	932	942	919	687	3161	502	543(8)	543.8(10)		450	
b_{1u}	13	3111	3173	3012	3029	3190						
	19a	1485	1511	1484	1440	1444						
	18a	1140	1157	1136	1144	1129						
	12	1019	1032	1021	776	896	931					
b_{2g}	5	978	981	983	925	928	620					
	4	770	763	756	634	682	709					
b_{2u}	20b	3039	3189	3063	3041	3204						
	15	1418	1436	1416	1398	1406						
	19b	1176	1185	1149	1144	1147						
	14	1068	1083	1063	957	970						
b_{3g}	7b	3008	3172	3040	3042	3183						
	3	1535	1566	1512	1593	1626						
	8b	1348	1367	1346	1282	1301						
	6b	712	707	704	630	630						
b_{3u}	11	794	805	785	773	779	830					
	16b	429	422	420	463	442	450				490	497(4)

[a] Innes et al.[49] [b] ZEKE via S_1 [ref 40]. [c] Nanosecond (2 + 1) REMPI [ref 21]. [d] Two color multiphoton ionization [ref 50]. [e] Based on tentative assignment. See Table 7.

TABLE 3: Vibrational Frequencies (cm^{-1}) of Pyrazine-D4 in S_0, D_0 and $3s(n^{-1})$ Rydberg State

		S_0		D_0		3s Rydberg
vibrational mode		B3LYP	Udagawa[a]	B3LYP	this work He(I) UPS	this work REMPI
a_g	2	2269		2290		
	8a	1533	1537	1419	1401(8)	1424(5)
	9a	1018	1005	1017	1051(16)	1004(15)
	1	884	884	851	847(8)	841(7)
	6a	593	586	580	615(8)	619(4)
a_u	17a	839		789		
	16a	289	286	335		
b_{1g}	10a	730	721	492	495(10)	464(17)
b_{1u}	13	2216		2257		
	19a	1359		1337		
	18a	1026		893		
	12	869		722		
b_{2g}	5	855	651	794		
	4	649	590	547		
b_{2u}	20b	2256		2256		
	15	1267		1336		
	19b	1191		1017		
	14	833		788		
b_{3g}	7b	2238		2232		
	3	1522		1587		
	8b	1030		981		
	6b	689		610		
b_{3u}	11	607	597	617		
	16b	409	398	423		

[a] Udagawa et al.[52]

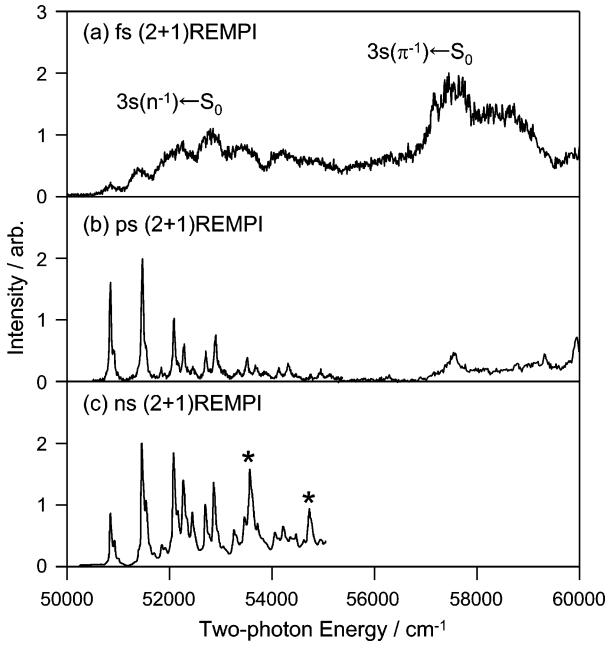

Figure 1. (2 + 1) resonance enhanced multiphoton ionization (REMPI) spectra of pyrazine-H4 observed via $3s(n^{-1})$ and 3s (π^{-1}) Rydberg with (a) a femtosecond laser (150−200 fs), (b) a picosecond laser (2.8 ps), and (c) a nanosecond laser. The spectra (a) and (c) were adapted from the reference 20 and 21, respectively. The spectrum (b) was measured in the present work by maintaining a constant laser power during the measurement. The spectra (a) and (b) are of molecules in a supersonic jet, while (c) is of a vapor.

The vibrational frequencies in the $3s(n^{-1})$ Rydberg state are expected to be similar to those in D_0. Therefore, the vibrational assignments of the (2 + 1) REMPI spectra of pyrazine-H4 and D4 were carried out referring to the vibrational frequencies in $D_0(n^{-1})$ calculated at the B3LYP/cc-pVTZ level. Figure 3 shows the (2 + 1) REMPI spectra in the $3s(n^{-1})$ region with vibrational assignments thus made. The spectra exhibit strong progressions of the 6a and 8a modes and weak combination bands between these modes and the 1 and 9 modes. The vibrational forms of these normal modes are also illustrated in Figure 3. Tables 4 and 5 summarize the vibrational energies, relative intensities, and assignments of the (2 + 1) REMPI spectra of pyrazine-H4 and D4, respectively. The fundamental vibrational frequencies are listed in Table 6. Since we measured the picosecond REMPI

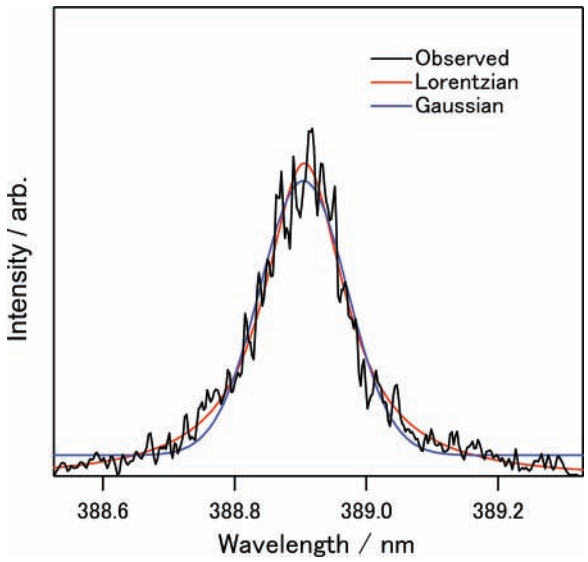

Figure 2. Line shape of $6a_0^1$ band of $3s(n^{-1}) \leftarrow S_0$ observed by a nanosecond laser in the present work. A least-squares fitting of a Lorentzian provides the width of 17(1) cm^{-1}.

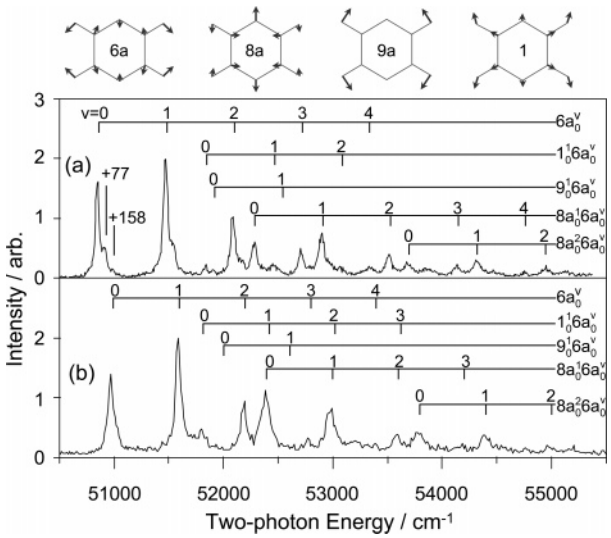

Figure 3. Expanded views of (2 + 1) picoseconds REMPI spectra of (a) pyrazine-H4 and (b) D4 with vibrational assignments.

spectra with a stabilized laser power, the observed band intensities are compared directly with calculated Franck−Condon intensities in a later section of this paper.

The two bands [marked in Figure 3a] seen in the high-energy side, at +77 and +158 cm^{-1}, of the band origin of pyrazine-H4 was also seen previously,[21] although no assignment has been made. We found that these bands disappear in a nanosecond (2 + 1) REMPI spectrum of pyrazine cooled in a pulsed supersonic jet, indicating that these are hot bands. We assigned them to 16 b_1^1 (+77) and $16b_2^2$ (+158) which yields the fundamental frequency of the 16b mode in the $3s(n^{-1})$ state to be 497 cm^{-1} when using 420 cm^{-1} for the frequency in S_0. The estimate of 497 cm^{-1} is in fair agreement with the frequency 480 cm^{-1} of 16b observed by Goto et al.[50] The $16b_0^2$ band was not seen in our spectrum.

Figure 4 shows the time-of-flight (TOF) mass spectra observed upon REMPI using nanosecond and picosecond lasers in the present work. Due to the impedance mismatch in the signal line, TOF peaks exhibit ringings. Nevertheless, one can see that the parent mass signal is predominantly observed by (a) nanosecond and (b) picosecond REMPI via $3s(n^{-1})$ zero

TABLE 4: Assignment of Vibrational Bands Observed in (2 + 1) REMPI of Pyrazine-H4

energy/cm^{-1}	vibrational energy/cm^{-1}	relative intensity	assignment
50844		1.000	0_0^0
50921	77	0.338	$16b_1^1$
51002	158	0.109	$16b_2^2$
51482	639	1.368	$6a_0^1$
51563	720	0.383	$16b_1^1 6a_0^1$
51650	806	0.101	$16b_2^2 6a_0^1$
51853	1010	0.138	1_0^1
51929	1085	0.095	$9a_0^1$
52116	1273	0.718	$6a_0^2$
52192	1349	0.217	$16b_1^1 6a_0^2$
52260	1417	0.118	$16b_2^2 6a_0^2$
52316	1472	0.382	$8a_0^1$
52399	1555	0.124	$16b_1^1 8a_0^1$
52486	1642	0.138	$1_0^1 6a_0^1$
52567	1723	0.091	$9a_0^1 6a_0^1$
52752	1909	0.321	$6a_0^3$
52837	1993	0.115	$16b_1^1 6a_0^3$
52932	2089	0.391	$8a_0^1 6a_0^1$
53009	2166	0.153	$16b_1^1 8a_0^1 6a_0^1$
53097	2253	0.071	$1_0^1 6a_0^2$
53179	2336	0.050	$9a_0^1 6a_0^2$
53374	2531	0.126	$6a_0^4$
53462	2618	0.075	$16b_1^1 6a_0^4$
53556	2712	0.226	$8a_0^1 6a_0^2$
53625	2782	0.081	$16b_1^1 8a_0^1 6a_0^2$
53697	2853	0.136	$1_0^1 6a_0^3$
53757	2914	0.070	$8a_0^2$
53837	2993	0.064	$9a_0^1 6a_0^3$
54190	3346	0.624	$8a_0^1 6a_0^3$
54273	3429	0.049	$1_0^1 6a_0^4$
54363	3519	0.139	$8a_0^2 6a_0^1$
54434	3591	0.054	$9a_0^1 6a_0^4$
57505			$3s(\pi^{-1})$

TABLE 5: Assignment of Vibrational Bands Observed in (2 + 1) REMPI of Pyrazine-D4

energy/cm^{-1}	vibrational energy/cm^{-1}	relative intensity	assignment
50997	0	1.000	0_0^0
51615	619	1.555	$6a_0^1$
51838	841	0.313	1_0^1
51924	927	0.100	$10a_0^2$
52001	1004	0.083	$9a_0^1$
52213	1216	0.669	$6a_0^2$
52421	1424	0.787	$8a_0^1$
52494	1497	0.219	$1_0^1 6a_0^1$
52576	1579	0.111	$10a_0^2 6a_0^1$
52656	1659	0.091	$9a_0^1 6a_0^1$
52812	1815	0.175	$6a_0^3$
53003	2006	0.641	$8a_0^1 6a_0^1$
53077	2080	0.247	$1_0^1 6a_0^2$
53399	2402	0.147	$6a_0^4$
53608	2611	0.287	$8a_0^1 6a_0^2$
53701	2705	0.139	$1_0^1 6a_0^3$
53877	2880	0.170	$8a_0^2$
54009	3013	0.098	$6a_0^5$
54204	3207	0.128	$8a_0^1 6a_0^3$
54406	3409	0.249	$8a_0^2 6a_0^1$
55008	4011	0.103	$8a_0^2 6a_0^2$
55215	4219	0.078	$8a_0^3$
57452			$3s(\pi^{-1})$

vibrational level, while weak fragment ion signals (m/e = 26 and 53) also exist. The intensity of the daughter ions increased in REMPI via the $6a^1$ level in comparison with REMPI via the 0° level as shown in Figure 4c. The result implies that the

TABLE 6: Comparison of the Experimental and Theoretical Vibrational Frequencies (cm^{-1}) of Pyrazine-H4 and D4 in Their D_0 and $3s(n^{-1})$ Rydberg States Obtained in the Present Study[a]

		pyrazine-H4				pyrazine-D4		
		D_0			$3s(n^{-1})$	D_0		$3s(n^{-1})$
vibrational mode		B3LYP	He(I) UPS	VUV−PFI-PE	REMPI	B3LYP	He(I) UPS	REMPI
a_g	2	3048		3050.6(10)		2290		
	8a	1439	1417(8)	1418.4(10)	1472(9)	1419	1401(8)	1424(5)
	9a	1192	1187(8)	1193.9(10)	1085(4)	1017	1051(16)	1004(15)
	1	1014	1010(8)	1004.8(10)	1010(9)	851	847(8)	841(7)
	6a	632	635(8)	635.8(10)	639(3)	580	615(8)	619(4)
b_{1g}	10a	687	543(8)	543.2(10)		492	495(10)	464(17)
b_{3u}	11	773				617		
	16b	463			497(4)	423		

[a] This work. The experimental He(I) UPS and VUV−PFI-PE values are based on assignments of the He(I) UPS and VUV−PFI-PE spectra. See Table 7.

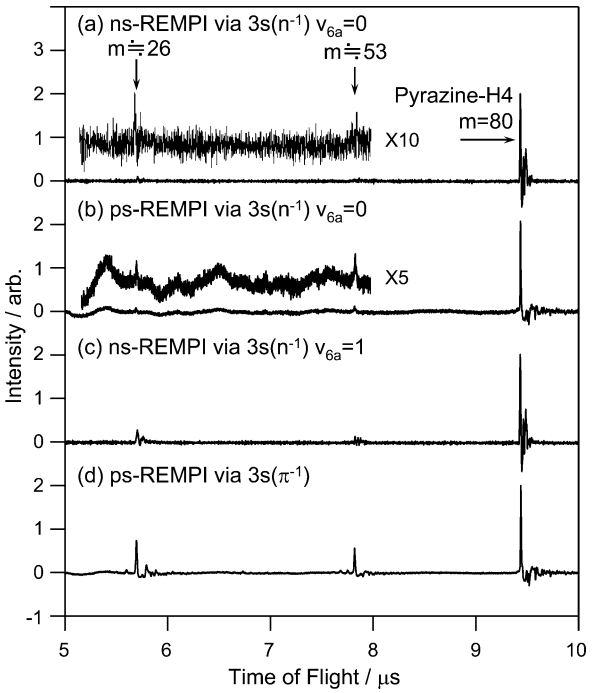

Figure 4. TOF-mass spectra (a) and (b) correspond to the resonance states of $v = 0$ of $3s(n^{-1})$ in nanosecond and picosecond (2 + 1) REMPI, respectively; (c) corresponds to the resonance state of $6a^1$ of $3s(n^{-1})$ in nanosecond (2 + 1) REMPI, and (d) corresponds to picosecond (2 + 1) REMPI via the $3s(\pi^{-1})$ Rydberg state.

relative band intensities in the (2 + 1) REMPI spectrum could depend on the particular mass monitored. However, we observed the total photoelectron signal in picosecond REMPI measurements shown in Figures 1−3 to avoid such complexity. Since the origin bandwidth of $3s(n^{-1})$ corresponds to the lifetime of 0.3 ps, suggesting that there is fast internal conversion from the 3s state to lower electronic states. If this internal conversion leads to dissociation of a molecule, the fragment ions at $m/e =$ 26 and 53 masses may be resulting from ionization of the neutral fragments. However, it is also possible that the fragment ions result from dissociative ionization of a parent molecule. These two possibilities can be discriminated in some favorable cases by observing speed and angular distributions of these fragment ions.[55] In the present work, we have not performed such measurements. The intensity of the pyrazine ion ($m/e = 80$) was found to depend on the 2.7th power of the laser intensity, whereas that of the fragment ion (mass $m/e = 26$) exhibited the 4.5th power dependency of the laser intensity in nanosecond REMPI measurements.

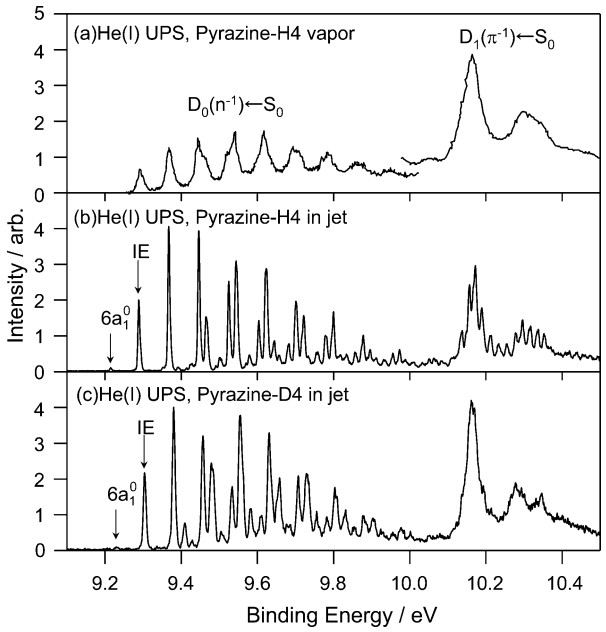

Figure 5. (a) He(I) photoelectron spectrum at room temperature reproduced from the literature[24] with energy recalibration by 83 meV (see the text). (b) He(I) UPS of pyrazine-H4 in a supersonic jet. The spectral resolution is 5.5 meV. (c) He(I) photoelectron spectrum of pyrazine-D4 in a supersonic jet.

B. High-Resolution He(I) UPS. Figure 5 compares (a) a He(I) photoelectron spectrum of pyrazine vapor from the literature,[24] (b) a high-resolution He(I) photoelectron spectrum of pyrazine-H4 in a supersonic jet, and (c) the corresponding spectrum of pyrazine-D4 measured in the present work. Vibrational bands appearing in 9.2−10.1 and 10.1−10.4 eV correspond to $D_0(n^{-1})$ and $D_1(\pi^{-1})$, respectively. Clearly, our new spectrum shown in (b) exhibits superior resolution compared to that of the old spectrum (a). When the spectrum (b) was convoluted with a Gaussian function with fwhm of 20 meV, its spectral feature agreed reasonably well with that of (a). For the reason discussed below, the spectrum shown in (a) has been shifted by 83 meV to align with our spectrum. Notice also that the spectral feature of the $D_1(\pi^{-1})$ region is dramatically different between pyrazine-H4 and -D4 in that fine splittings of the bands are seen only for the spectrum (b) of pyrazine-H4, which will be discussed in more detail later.

We have determined the term value of the $D_0(n^{-1})$ state, ionization energy (IE) of pyrazine-H4, to be 9.288(1) eV, which is in reasonable agreement with 9.2875 eV obtained by PFI-PE spectroscopy via S_1[40] and the convergence limit of Rydberg series, 9.2883(6) eV.[56] On the low-energy side of the origin

band, there appears a hot band $6a_1^0$ both for pyrazine-H4 and D4. The shape of the origin band of $D_0(n^{-1})$ of pyrazine-H4 exhibited asymmetric shading toward the high-energy side, which is ascribed to the overlap with the $6a_1^1$ (+42 cm^{-1}) and $6a_2^2$ (+90 cm^{-1}) hot bands. It is not clear why 16b appears as a hot band in (2 + 1) REMPI via 3s, whereas 6a appears in He(I) UPS. In the region of $D_0(n^{-1})$, the line width was constant within our experimental error. The observed line width of the $D_0(n^{-1})$ origin band of pyrazine-D4 was 9 meV, slightly wider than that of pyrazine-H4. However, this was simply due to contamination of the energy analyzer when the measurement of pyrazine-D4 was carried out.

The term value in $D_1(\pi^{-1})$ of pyrazine-H4 was determined to be 10.169(1) eV. As for pyrazine-D4, the term values of $D_0(n^{-1})$ and $D_1(\pi^{-1})$ were determined to be 9.304(1) and 10.164-(1) eV, respectively. The energy differences between D_1 and D_0 are 881 meV (7106 cm^{-1}) in pyrazine-H4 and 860 meV (6936 cm^{-1}) in pyrazine-D4. This relation is parallel to the electronic energy gap between $3s(\pi^{-1})$ and $3s(n^{-1})$ of 6661 and 6465 cm^{-1} in pyrazine-H4 and -D4, respectively, determined by (2 + 1) REMPI. In both cases of pyrazine-H4 and -D4, the electronic energy gap between n^{-1} and π^{-1} is smaller in the 3s state than in the cation by as large as 400 cm^{-1}.

Fridh et al.[24] have reported an IE value of 9.216(1) for pyrazine-H4, which is considerably lower than our value. Since the second vibronic band in their spectrum is at 9.291 eV, we first considered their lowest band at 9.216(1) eV to be a hot band from the $6a_1$ level in S_0 and the second lowest band at 9.291 eV as the true 0_0^0 band of $D_0 \leftarrow S_0$. Åsbrink et al.[23] have reported essentially the same spectrum with the one by Fridh et al.,[24] yet with a slightly higher resolution. We examined the spectrum of Åsbrink et al. more closely and found that their spectral feature agrees quite well with ours when their spectrum is shifted toward a higher energy by about 83 meV. Thus, it seemed likely that their photoelectron energy calibration for this particular spectrum was incorrect for some unknown reasons. We have also examined a photoelectron spectrum of benzene reported by Åsbrink et al.,[23] and we found that the spectrum is in excellent agreement with our spectrum of benzene in a supersonic jet, not shown here, and with the one by Baltzer et al.[57] Therefore, if there is any problem in their energy calibration, it is perhaps specific to the pyrazine spectrum by Åsbrink et al.[23] In order to simulate the effect of hot bands under the condition employed by Åsbrink et al., we have carried out Franck−Condon simulation as shown in Figure 6. We concluded that the hot band from the $6a_1$ level in S_0 should not appear as strongly as the cold band in the spectrum at a room temperature. Thus, the first vibronic band in the He(I) spectra by Åsbrink et al.[23] and Fridh et al.[24] should be the 0_0^0 band of $D_0 \leftarrow S_0$, and the entire spectra in the D_0 region need to be shifted by about 83 meV to the higher energy. From the Franck−Condon simulation of our UPS spectrum, we estimated the vibrational temperature of pyrazine-H4 in our CW supersonic jet to be 277 K, which is near the room temperature (298 K).

The vibrational assignments in the $D_0(n^{-1})$ region are shown in Figure 7, panels b and c, respectively, along with theoretical prediction of the spectrum in (a). The prominent vibrational progressions, the totally symmetric in-plane bending mode 6a and combination bands with other totally symmetric vibrational modes (8a, 9a, and 1) were clearly identified in the spectra. The vibrational frequencies derived from the He(I) UPS spectrum along with the calculated values and the VUV−PFI-PE values (see section IV.D) are summarized in Table 6. For the totally symmetric 6a, 8a, 1, and 9a modes, our He(I)

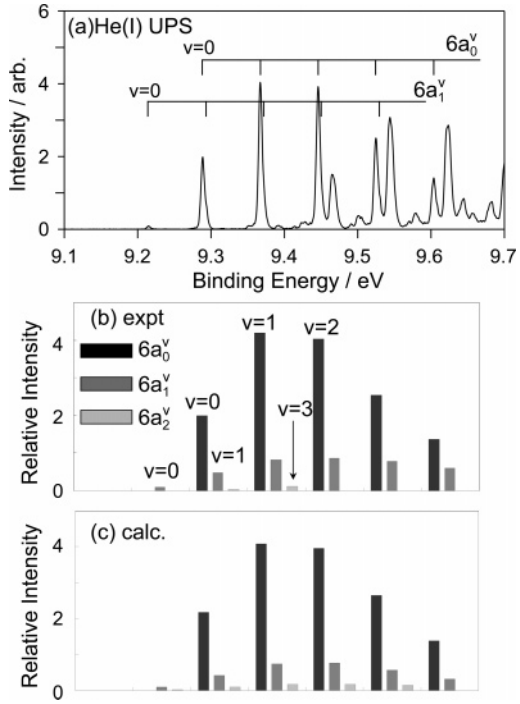

Figure 6. (a) Expanded views of He(I) UPS of pyrazine-H4 with vibrational assignments of hot bands. (b) and (c) correspond to observed and simulated relative intensities at a room temperature of He(I) photoelectron spectrum of pyrazine-H4, respectively.

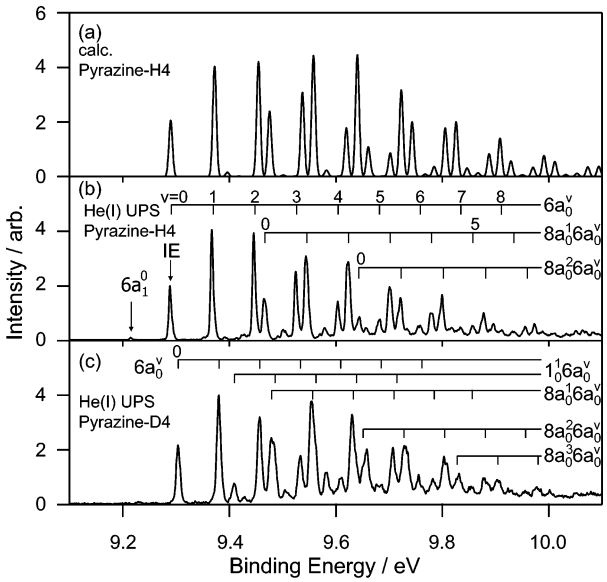

Figure 7. (a) Expanded views of simulated He(I) photoelectron spectrum in the $D_0(n^{-1}) \leftarrow S_0$ region obtained by the B3LYP/ cc-pVTZ level of calculations for pyrazine-H4. The line width of fwhm of 6 meV was assumed. (b) Observed He(I) photoelectron spectrum of pyrazine-H4 in a supersonic jet with vibrational assignments (c) The He(I) photoelectron spectrum of pyrazine-D4.

experimental values are in good agreement with the values from DFT at the B3LYP/cc-pVTZ level. The He(I) frequencies of 6a, 1, and 9a modes also agree with the literature, although we need to correct the assignment of the 8a mode made previously.[40] The value of the $10a(b_{1g})$ mode, the out-of-plane hydrogen bending, calculated at the B3LYP/cc-pVTZ level did not reproduce with the experimental value very well, which is attributed to inaccuracy in DFT calculation. This might be understandable, as the 10a mode is responsible for the vibronic coupling between $D_0(n^{-1})$ and $D_1(\pi^{-1})$. Tables 7 and 8 list the

TABLE 7: Energies of Vibrational Bands Observed in the He(I)UPS and VUV-PFI-PE Spectra of Pyrazine-H4 and Their Assignments[a]

He(I)UPS			VUV-PFI-PE			
energy/ eV	vibrational energy/cm^{-1}	relative intensity	energy[b]/ cm^{-1}	energy/ eV	vibrational energy[c]/cm^{-1}	assignment
9.215	−593	0.046	74312.9	9.21363	−593.7	$6a_1^0$
9.288	0	1.000	74906.6	9.28724	0	0_0^0
9.294	42	0.245	74946.3	9.29216	39.7	$6a_1^1$
9.300	90	0.017				$6a_2^2$
9.367	635	2.093	75542.4	9.36607	635.8	$6a_0^1$
9.372	677	0.415	75579.5	9.37067	672.9	$6a_1^2$
			75617.6	9.37539	711.0	Y_0^1
9.378	723	0.061				$6a_2^3$
9.414	1010	0.042	75911.4	9.41182	1004.8	1_0^1
9.423	1087	0.086	75993.0	9.42194	1086.4	$10a_0^2$
			76037.5	9.42745	1130.9	$10a_0^2 6a_1^1$
9.436	1187	0.085	76100.5	9.43526	1193.9	$9a_0^1$
9.446	1270	2.013	76176.0	9.44462	1269.4	$6a_0^2$
9.451	1313	0.436	76213.8	9.44931	1307.2	$6a_1^3$
			76255.3	9.45446	1348.7	$Y_0^1 6a_0^1$
9.464	1417	0.698	76325.0	9.46310	1418.4	$8a_0^1$
9.469	1455	0.567	76360.9	9.46755	1454.3	Y_0^2
9.474	1498	0.130	76396.1	9.47191	1489.5	$Y_0^2 6a_1^1$
9.491	1636	0.080	76543.9	9.49024	1637.3	$1_0^1 6a_0^1$
9.500	1707	0.197	76618.1	9.49944	1711.5	$10a_0^2 6a_0^1$
			76664.5	9.50519	1757.9	$10a_0^2 6a_1^2$
9.506	1754	0.156	76721.4	9.51225	1814.8	$9a_0^1 6a_0^1$
9.525	1905	1.274	76812.1	9.52349	1905.5	$6a_0^3$
9.530	1947	0.394	76849.6	9.52814	1943.0	$6a_1^4$
			76886.4	9.53270	1979.8	$Y_0^1 6a_0^2$
9.542	2049	1.349	76957.2	9.54148	2050.6	$8a_0^1 6a_0^1$
9.547	2085	1.148	76991.8	9.54577	2085.2	$Y_0^2 6a_0^1$
9.552	2128	0.257	77023.3	9.54967	2116.7	$Y_0^2 6a_1^2$
9.570	2270	0.123	77176.9	9.56872	2270.3	$1_0^1 6a_0^2$
9.578	2335	0.234	77240.8	9.57664	2334.2	$10a_0^2 6a_0^2$
			77263.0	9.57940	2356.4	$9a_0^2$
			77286.1	9.58226	2379.5	$10a_0^2 6a_1^3$
9.584	2380	0.154	77360.4	9.59147	2453.8	$9a_0^1 6a_0^2$
			77410.6	9.59770	2504.0	$8a_0^1 10a_0^2$
9.603	2538	0.689	77447.3	9.60225	2540.7	$6a_0^4$
9.608	2577	0.298	77483.3	9.60671	2576.7	$6a_1^5$
			77521.8	9.61148	2615.2	$Y_0^1 6a_0^3$
9.621	2678	1.238	77588.0	9.61969	2681.4	$8a_0^1 6a_0^2$
9.625	2716	1.218	77623.3	9.62407	2716.7	$Y_0^2 6a_0^2$
9.631	2761	0.295	77661.2	9.62877	2754.6	$Y_0^2 6a_1^3$
9.638	2820	0.264	77733.3	9.63771	2826.7	$8a_0^2$
9.644	2867	0.440	77776.0	9.64300	2869.4	Y_0^4
			77813.2	9.64761	2906.6	$1_0^1 6a_0^3$
9.649	2911	0.190				$6a_1^1 Y_0^4$
9.656	2966	0.240	77864.5	9.65397	2957.9	$10a_0^2 6a_0^3$
			77889.7	9.65710	2983.1	$9a_0^2 6a_0^1$
			77905.5	9.65906	2998.9	$10a_0^2 6a_1^4$
			77957.2	9.66547	3050.6	2_0^1
			77992.0	9.66978	3085.4	$9a_0^1 6a_0^3$
			78044.2	9.67625	3137.6	$8a_0^1 10a_0^2 6a_0^1$
9.682	3178	0.389	78080.2	9.68072	3173.6	$6a_0^5$
			78153.7	9.68983	3247.1	$Y_0^1 6a_0^4$
9.699	3312	0.764	78220.0	9.69805	3313.4	$8a_0^1 6a_0^3$
9.703	3347	0.782	78254.2	9.70229	3347.6	$Y_0^2 6a_0^3$
9.709	3389	0.270	78290.3	9.70676	3383.7	$Y_0^2 6a_1^4$
9.716	3448	0.443	78360.4	9.71546	3453.8	$8a_0^2 6a_0^1$
9.722	3493	0.749	78404.8	9.72096	3498.2	$Y_0^4 6a_0^1$
			78444.1	9.72583	3537.5	$1_0^1 6a_0^4$
			78484.2	9.73081	3577.6	$10a_0^2 6a_0^4$
			78510.9	9.73412	3604.3	$9a_0^2 6a_0^2$
			78663.9	9.75309	3757.3	$8a_0^1 10a_0^2 6a_0^2$
9.759	3794	0.262	78710.4	9.75885	3803.8	$6a_0^6$
9.777	3941	0.453	78852.5	9.77647	3945.9	$8a_0^1 6a_0^4$
9.782	3982	0.438	78887.7	9.78083	3981.1	$Y_0^2 6a_0^4$
			78926.5	9.78564	4019.9	$Y_0^2 6a_1^5$
9.794	4079	0.420	78992.0	9.79376	4085.4	$8a_0^2 6a_0^2$
9.800	4123	0.796	79034.8	9.79907	4128.2	$Y_0^4 6a_0^2$
9.819	4279	0.206				$8a_0^3$
9.824	4323	0.139				Y_0^6

TABLE 7: (Continued)

He(I)UPS			VUV-PFI-PE			
energy/ eV	vibrational energy/cm^{-1}	relative intensity	energy[b]/ cm^{-1}	energy/ eV	vibrational energy[c]/cm^{-1}	assignment
9.834	4402	0.200				$6a_0^7$
9.856	4576	0.250	79481.5	9.85445	4574.9	$8a_0^1 6a_0^5$
9.861	4616	0.184	79519.0	9.85910	4612.4	$Y_0^2 6a_0^5$
			79547.8	9.86268	4641.2	$Y_0^2 6a_1^6$
9.873	4711	0.290	79618.2	9.87140	4711.6	$8a_0^2 6a_0^3$
9.878	4755	0.490	79664.5	9.87714	4757.9	$Y_0^4 6a_0^3$
9.896	4896	0.317				$8a_0^3 6a_0^1$
9.901	4942	0.159				$Y_0^6 6a_0^1$
9.913	5033	0.181				$6a_0^8$
9.930	5177	0.142				$8a_0^1 6a_0^6$
9.936	5219	0.137				$Y_0^2 6a_0^6$
9.956	5385	0.229				$8a_0^2 6a_0^4$
9.961	5425	0.093				$Y_0^4 6a_0^4$
9.972	5517	0.275				$8a_0^3 6a_0^2$
9.977	5552	0.148				$Y_0^6 6a_0^2$
9.989	5647	0.154				$6a_0^9$
10.012	5833	0.125				$8a_0^1 6a_0^7$
10.032	5999	0.115				$8a_0^2 6a_0^5$
10.050	6143	0.167				$8a_0^3 6a_0^3$
10.055	6184	0.115				$Y_0^6 6a_0^3$
10.064	6255	0.128				$6a_0^{10}$
10.089	6460	0.119				$8a_0^1 6a_0^8$

[a] This work. [b] The uncertainties of vibrational PFI-PE band energies are ±2 cm^{-1}. [c] Vibrational energies measured with respected to the origin band. The uncertainties are ±1 cm^{-1}.

IE values, vibrational energies, relative intensities, and assignments of the photoelectron spectra of pyrazine-H4 and -D4, respectively.

In order to predict a photoelectron spectrum shown in Figure 7b theoretically, we have carried out computations of the Franck−Condon factors (FCFs) following the procedure reported by Chen et al.[58−61] that is based on the methods by Sharp and Rosenstock[62] and Hutchisson.[63] The normal coordinates in the ground state and in the cationic state are not identical when there is a geometrical change (Duschinsky effect).[64] In such a case, calculations of the FCFs require coordinate transformation

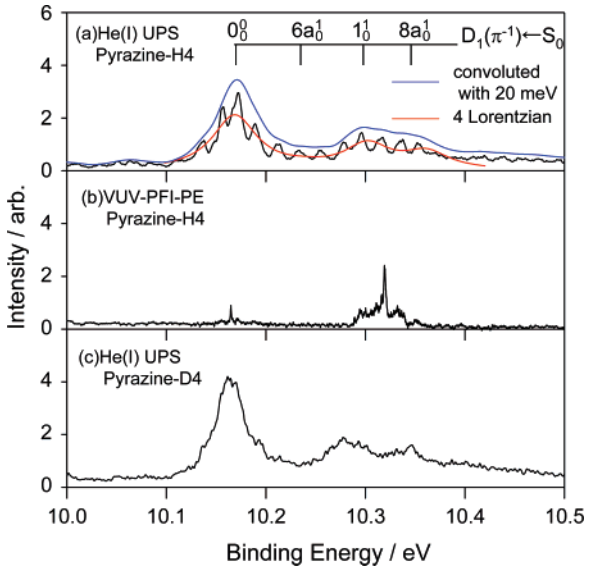

Figure 8. (a) Expanded view of He(I) hotoelectron spectrum of jet-cooled pyrazine-H4 with vibrational assignments in the $D_1(\pi^{-1}) \leftarrow S_0$ region. (b) VUV-PFI-PE spectrum of pyrazine-H4 in the $D_1(\pi^{-1}) \leftarrow S_0$ region. (c) He(I) photoelectron spectrum of pyrazine-D4 in a supersonic jet.

for one of these states. The transformation is expressed as

$$\mathbf{Q}' = \mathbf{JQ} + \mathbf{K} \quad (1)$$

where $\mathbf{Q}'$ and $\mathbf{Q}$ are the 3N-6 normal coordinates for the neutral and the cationic ground states and $\mathbf{J}$ and $\mathbf{K}$ are the $(3N - 6) \times (3N - 6)$ matrix and the $3N - 6$ column vector, respectively. Here, N is the number of atoms in a nonlinear molecule. In our FCF calculation, a harmonic approximation was employed. Figure 7a shows the simulated spectrum based on quantum chemical calculation at the B3LYP/cc-pVTZ level. The calculated spectrum qualitatively reproduces the FCFs of the 6a and 8a modes. However, closer inspection reveals discrepancies in band intensities between the experimental and calculated spectra. We note that the discrepancies in band positions originate from the harmonic approximation employed in the simulation.

An expanded view of the vibrational structure in the $D_1(^2B_{1g})$ region is shown in Figure 8. As we have not calculated vibrational frequencies for D_1, we have assigned these bands using the vibrational frequencies calculated for the neutral ground state at the B3LYP/cc-pVTZ level. The three bands correspond to vibrational energies of 67 (536), 127 (1016), and 179 meV (1432 cm^{-1}). These bands are estimated to appear at 61 (488), 117 (936), and 176 meV (1408 cm^{-1}) for pyrazine-D4. The B3LYP/cc-pVTZ calculation provides vibrational frequencies of 6a, 1, and 8a modes to be 604, 1025, and 1571 for pyrazine-H4 and 593, 884, and 1533 cm^{-1} for pyrazine-D4 in S_0. From these results, the vibronic bands associated with $D_1(\pi^{-1}) \leftarrow S_0$ were tentatively assigned to the fundamentals of the 6a, 1, and 8a modes. As shown in Figure 8a, the overall spectral feature was well reproduced by assuming four Lorentzian functions with fwhm of 55 meV. This homogeneous broadening corresponds to the lifetime of 12 fs. This value is consistent, and accidentally match with the one estimated by Seidner et al. who have computed the conical intersection of the $D_0(n^{-1})$ and $D_1(\pi^{-1})$ potential-energy surfaces including the coordinates of the modes 1, 6a, 8a, and 10a and deduced the lifetime of $D_1(\pi^{-1})$ to be 12 fs from phenomenological spectral

TABLE 8: Assignment of Vibrational Bands Observed in the He(I)UPS of Pyrazine-D4

energy/eV	vibrational energy/cm^{-1}	relative intensity	assignment
9.231	−589	0.033	$6a_1^0$
9.304	0	1.000	0_0^0
9.380	615	1.830	$6a_0^1$
9.409	847	0.372	1_0^1
9.427	989	0.102	$10a_0^2$
9.434	1051	0.043	$9a_0^1$
9.457	1231	1.516	$6a_0^2$
9.478	1401	0.973	$8a_0^1$
9.485	1461	0.799	$1_0^1 6a_0^1$
9.504	1614	0.206	$10a_0^2 6a_0^1$
9.512	1676	0.124	$9a_0^1 6a_0^1$
9.534	1851	0.724	$6a_0^3$
9.554	2014	1.718	$8a_0^1 6a_0^1$
9.562	2079	0.909	$1_0^1 6a_0^2$
9.610	2471	0.446	$6a_0^4$
9.630	2630	1.490	$8a_0^1 6a_0^2$
9.639	2699	0.637	$1_0^1 6a_0^3$
9.650	2791	0.534	$8a_0^2$
9.678	3012	0.299	X_0^1
9.687	3086	0.303	$6a_0^5$
9.707	3248	0.928	$8a_0^1 6a_0^3$
9.716	3325	0.362	$1_0^1 6a_0^4$
9.727	3408	0.856	$8a_0^2 6a_0^1$
9.755	3635	0.455	$X_0^1 6a_0^1$
9.764	3711	0.249	$6a_0^6$
9.783	3863	0.400	$8a_0^1 6a_0^4$
9.792	3939	0.232	$1_0^1 6a_0^5$
9.802	4018	0.711	$8a^2 6a_0^2$
9.823	4182	0.339	$8a_0^3$
9.832	4257	0.493	$X_0^1 6a_0^2$
9.842	4342	0.235	$6a_0^7$
9.854	4436	0.327	$8a_0^1 6a_0^5$
9.865	4525	0.208	$1_0^1 6a_0^6$
9.878	4627	0.457	$8a_0^2 6a_0^3$
9.900	4810	0.398	$8a_0^3 6a_0^1$
9.910	4885	0.348	$X_0^1 6a_0^3$
9.924	5001	0.283	$8a_0^1 6a_0^6$
9.936	5099	0.219	$1_0^1 6a_0^7$
9.950	5212	0.206	$8a_0^2 6a_0^4$
9.974	5406	0.301	$8a_0^3 6a_0^2$
9.985	5490	0.248	$X_0^1 6a_0^4$
9.999	5606	0.229	$8a_0^1 6a_0^7$
10.010	5691	0.166	$1_0^1 6a_0^8$
10.023	5794	0.172	$8a_0^2 6a_0^5$
10.051	6023	0.229	$8a_0^3 6a_0^3$
10.065	6135	0.202	$X_0^1 6a_0^5$
10.079	6249	0.243	$8a_0^1 6a_0^8$

fitting of the He(I) spectrum of pyrazine vapor.[25] Our new He-(I) spectrum resolved fine spectral feature in the $D_1(\pi^{-1})$ band, only for pyraizne-H4. These clamps are due to the doorway states in D_0 that are strongly coupled with the zero-order vibronic level in D_1. The width of each clamp is 11(3) meV that is larger than that of our instrumental resolution. From this width, we estimated that the intramolecular vibrational energy redistribution (IVR) from the doorway vibrational state of D_0 to the bath states takes place in 60 fs (a lower bound for the lifetime). The line width in the spectrum of $D_1(^2B_{1g})$ of pyrazine-D4 was estimated to be 44 meV (lifetime: 15 fs), which suggested that the $D_1 \rightarrow D_0$ internal conversion rate of pyraine-D4 is lower than that of pyrazine-H4.

The fine structures seen for pyrazine-H4 are missing for pyrazine-D4, which suggests that intrinsic line width of doorway states in D_0 is larger in D4 than in H4. Thus, it seems likely that IVR rate in the cationic ground state of pyrazine-D4 is higher than that of pyrazine-H4. However, it should be noted that the He(I) spectrum of pyrazine-D4 was measured with the instrumental resolution of 9 meV that is worse than 5.5 meV

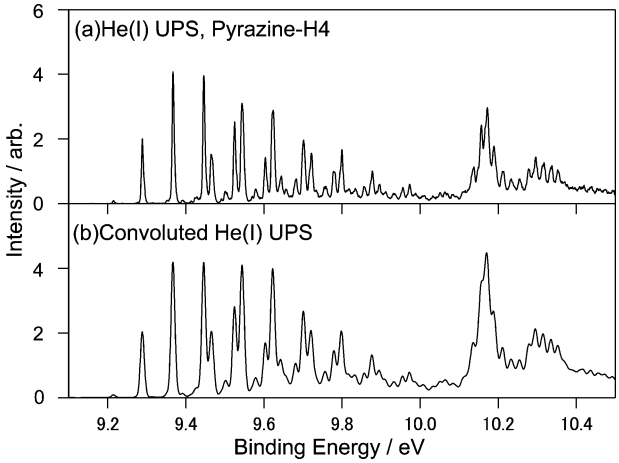

Figure 9. (a) He(I) photoelectron spectrum of pyrazine-H4 (b) He(I) photoelectron spectrum of pyrazine-H4 convoluted with a Gaussian function with fwhm of 9 meV.

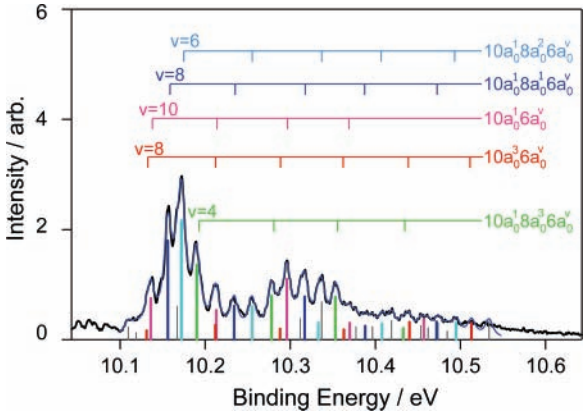

Figure 10. He(I) photoelectron spectrum of pyrazine-H4 with the assignments of the doorway vibrational states.

for pyrazine-H4. In order to examine the effect of spectral resolution, we have convoluted the He(I) photoelectron spectrum of pyrazine-H4 using a Gaussian function with a fwhm of 9 meV as shown in Figure 9. As seen here, the structures of doorway states are noticeable even at the spectral resolution of 9 meV, indicating that the doorway states in pyrazine-D4 have much wider linewidths and/or much higher densities.

Using the vibrational frequencies determined for D_0, we attempted assigning the doorway states appearing in the He(I) UPS of pyrazine-H4 as shown in Figure 10. As indicated, most of the bands are assigned as combination bands with one quantum of the mode 10a and several quanta of the modes 6a and 8a. Considering the symmetry of the D_1 and D_0 electronic states, the doorway states must have odd quanta of the mode 10a.

C. Picosecond Photoelectron Images via the Rydberg State. Figure 11 shows one-color (2 + 1) REMPI photoelectron images via the vibronic levels of the $3s(n^{-1})$ $\upsilon_{6a} = 0-3$ states. The observed images were processed using the inverse Abel transform, so that images correspond to the slices through the 3D photoelectron scattering distributions. The polarization vector of the laser beam (ϵ) is aligned vertically in the image plane. As seen in Figure 11, the photoelectron images exhibit one bright ring and some dark rings. The bright ring corresponds to the $\Delta\upsilon = 0$ transition: since the Rydberg state and the cationic state have similar molecular structures, the $\Delta\upsilon = 0$ propensity rule generally holds in ionization from the Rydberg state.

The photoelectron kinetic energy distributions (PKEDs) extracted from the images in Figure 11 after photoelectron

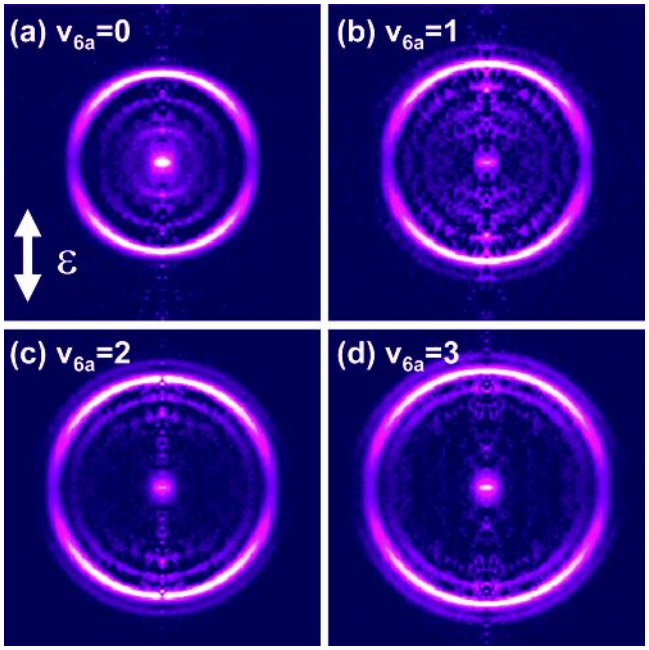

Figure 11. Photoelectron images in one-color picosecond (2 + 1) REMPI of jet-cooled pyrazine-H4 via $\upsilon_{6a} = 0-3$ levels in 3s(n^{-1}) state. These images correspond to slices through 3D photoelectron distributions. The laser polarization lies vertical in the imaging plane. The brightest rings in these images correspond to $\Delta\upsilon = 0$ transition upon ionization while faint rings are due to $\Delta\upsilon = \pm 1$ transitions. See the text.

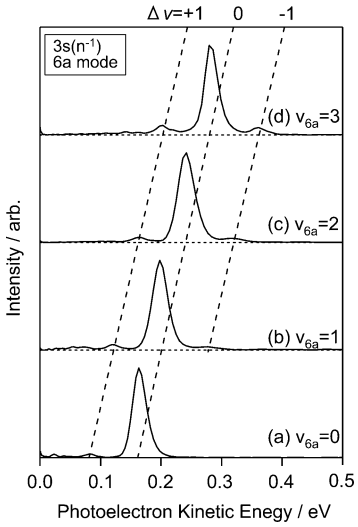

Figure 12. Photoelectron kinetic energy distributions extracted from the photoelectron images shown in Figure 11. Panels a−d correspond to the resonance states of 0, $6a^1$, $6a^2$, and $6a^3$ in 3s(n^{-1}) of pyrazine-H4, respectively.

kinetic energy calibration using (3 + 1) REMPI of Xe as presented in Figure 12. The PKE linearly shifts with the photon energy ($\hbar\omega$) in accordance with the following equation:

$$T_{\text{Rydberg}} + E_{\text{Rydberg}} + \hbar\omega = \text{IE} + E_{\text{cation}} + \text{PKE} \qquad (2)$$

where E_{cation} and E_{Rydberg} are the vibrational energies in the cation and the Rydberg state, respectively, and T_{Rydberg} is the term value of the Rydberg state. Since the vibrational frequencies in the cationic ground state and the Rydberg state are almost the same, $E_{\text{cation}} \approx E_{\text{Rydberg}}$, for the $\Delta\upsilon = 0$ band, we obtain

$$\text{PKE} = T_{\text{Rydberg}} + \hbar\omega - \text{IE} = \hbar\omega - \frac{R}{(n-\delta)^2} \qquad (3)$$

where R is the Rydberg constant, n is the principal quantum number of the Rydberg state, and δ is the quantum defect. The $\Delta\upsilon = 0$ band followed eq 3, and the term value and the quantum defect of 3s(n^{-1}) were determined to be 50 846 cm^{-1} and 0.86, respectively. The term value is in excellent agreement with a more accurate value, 50 844 cm^{-1}, by (2 + 1) REMPI described in section IV A. Two adjacent peaks on both sides of the main peak in the PKED via the 3s(n^{-1}, $\upsilon_{6a} = 3$) state are separated by 77(1) and 81(1) meV, respectively, which agree with the vibrational frequency of the 6a mode (78.7 meV) in $D_0(n^{-1})$ obtained by our He(I) UPS. Thus, these small peaks are assigned to $\Delta\upsilon_{6a} = -1$ and +1. Other photoelectron images via the 3s(n^{-1}, $\upsilon_{6a} = 0, 1, 2$) also exhibited clearly the $\Delta\upsilon_{6a} = -1$ and +1 transitions.

The photoelectron angular distribution (PAD) in the three-photon ionization can be generally described in terms of the expansion up to the sixth order Legendre polynomial. However, STS have already found that the contribution of the sixth order Legendre term is negligible in this case.[20] Thus, PAD $I(\theta)$ is given by

$$I(\theta) = \frac{\sigma}{4\pi}[1 + \beta_2 P_2(\cos\theta) + \beta_4 P_4(\cos\theta)] \qquad (4)$$

where σ is a photoionization cross-section, θ is the angle measured with respect to the light polarization, P_k is the kth order Legendre polynomial, and β_k is the anisotropy parameter. Figure 13 shows PAD and the anisotropy parameters extracted from the photoelectron images shown in Figure 11. The anisotropy parameters are in fair agreement with those obtained by STS.[20]

D. VUV-PFI-PE Spectrum and Its Vibrational Assignment. Figure 14 depicts the VUV−PFI-PE spectrum of pyrazine-H4 in the 9.17−10.20 eV. The resolution achieved of the VUV−PFI-PE spectrum is 1.5 cm^{-1} (fwhm) and is clearly superior to that of the He(I) UPS. The Stark shift of the IE is found to be 1.7 cm^{-1}. The energy scale of the VUV−PFI-PE spectra of Figure 14 and vibrational band positions listed in Table 7 have been corrected for this Stark shift. The shape of the $D_0(n^{-1})$ origin band of pyrazine-H4 is well approximated by a Gaussian function with a fwhm of 10 cm^{-1}. In fact, all PFI-PE vibrational bands of the $D_0(n^{-1})$ are found to have essentially the same fwhm of ≈10 cm^{-1}. On the basis of the peak position of the PFI-PE origin band, the adiabatic IE was determined to be 74 906.6 ± 2.0 cm^{-1} (9.287 28 ± 0.000 25 eV). Here, the uncertainty of ±2.0 cm^{-1} assigned for the IE has taken into account the optical resolution of the VUV laser and VUV energy calibration.

A marked difference of the VUV−PFI-PE spectrum shown in Figure 14 from the photoelectron spectrum in Figure 5 is a missing feature of $D_1(\pi^{-1})$. An expanded view of the D_1 region is shown in Figure 8b. The VUV−PFI-PE spectrum exhibits some sharp bands in the region, yet these features are completely different from those observed in the He(I) UPS. To our knowledge, this is the first clear example, which shows that the VUV−PFI-PE band can differ significantly from the He(I) UPS, possibly due to the short lifetime of the high-n Rydberg states involved in the VUV−PFI-PE measurement.

Figure 15 compares spectral features in UPS and VUV−PFI-PE more closely. Notice that almost all bands observed by VUV−PFI-PE in the $D_0(n^{-1})$ region were identical with those in the He(I) UPS, although close comparison reveals that the

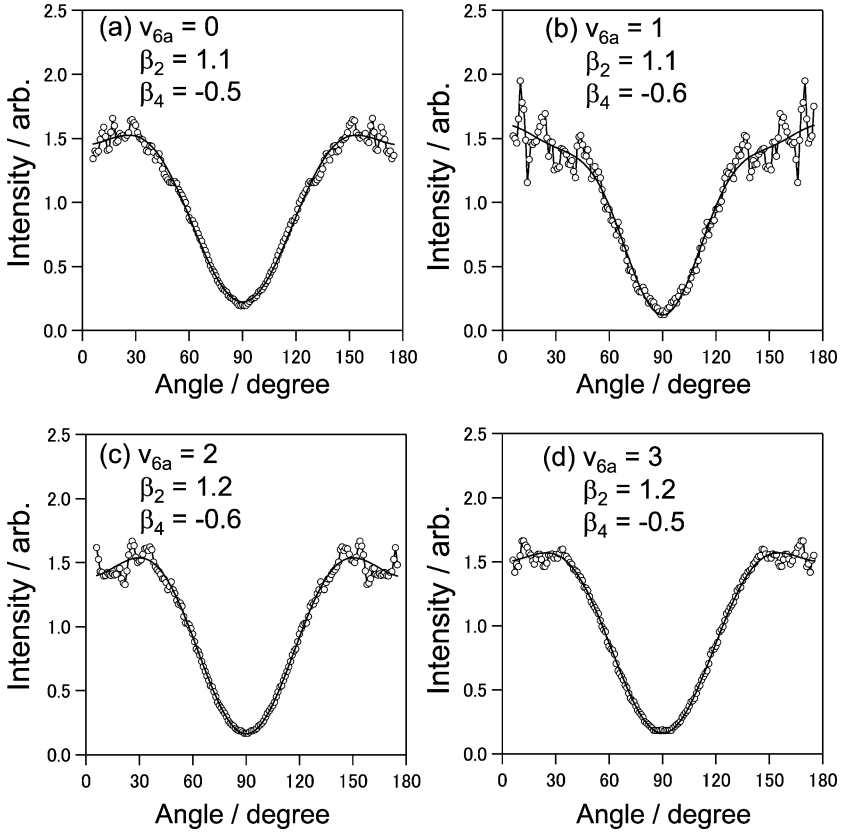

Figure 13. Photoelectron angular distributions extracted from the photoelectron images shown in Figure 11. Panels a−d correspond to the resonance states of 0, $6a^1$, $6a^2$, and $6a^3$ in $3s(n^{-1})$ of pyrazine-H4, respectively.

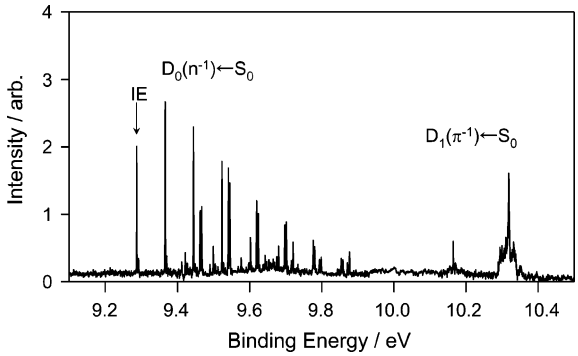

Figure 14. VUV-PFI-PE spectrum of pyrazine-H4 in a supersonic jet.

vibrational temperature is lower in the VUV−PFI-PE spectrum, which is ascribed to pulsed expansion of a sample gas, giving rise to small difference in the hot band feature. The vibrational frequencies in D_0 were determined more accurately with VUV−PFI-PE as summarized in Table 6. Especially, the 10a, 1, and 9a bands are overlapping with other bands in the He(I) photoelectron spectrum, while these bands are well resolved in VUV−PFI-PE. The frequencies of 6a and 8a modes agree well with the values obtained by He(I) UPS. The band shape of $8a_0^1$ in He(I) photoelectron spectrum indicated that this band is overlapping with another vibronic band (named Y), which is unambiguously resolved in VUV-PFI-PE. The fundamental frequency of the mode Y is 728(2) cm^{-1}, and this mode does not seem to be the a_g symmetry. The candidates for this vibrational mode are 12 (b_{1u}), 11 (b_{3u}), and 4 (b_{2g}) modes. We could not observe the corresponding band for pyrazine-D4. Since the PFI-PE method is subject to mediation of near resonance autoionizing Rydberg states, vibrational bands with negligible FCFs can often be observed in VUV-PFI-PE studies. Thus, it is not surprising to find that some vibrational bands resolved in the VUV-PFI-PE spectrum are not observed in the He(I) UPS (see detailed assignments in Table 7).

E. One-Dimensional Franck−Condon Simulation. Spectral simulations purely based on quantum chemical calculations were qualitatively yet not quantitatively accurate as shown in Figure 7, panels a and b. Instead of exploring further higher levels of quantum chemical calculations to improve the simulation, we have employed one-dimensional Franck−Condon analysis of the experimental results based on the following approximations using 3N-6 harmonic oscillator wavefunctions for determining the structure of D_0

$$\psi = \psi_1(Q_1)\psi_2(Q_2)\psi_3(Q_3)\cdots\psi_{3N-6}(Q_{3N-6}) \qquad (5)$$

The He(I) UPS and (VUV−PFI-PE spectrum) exhibited the vibrational spacings of $\upsilon_{6a} = 0-1$, $1-2$, $2-3$, and $3-4$ to be 635 (636), 636 (634), 635 (635), and 633 (633) cm^{-1}, respectively. Similarly, the (2 + 1) REMPI spectrum revealed the vibrational spacings of 639, 634, and 636 cm^{-1} with the accuracy of 8 cm^{-1}. Thus, the one-dimensional potential for the 6a mode seems rather harmonic in both the 3s Rydberg state and D_0. For the 8a mode, the vibrational spacings for $\upsilon_{8a} = 0-1$, $1-2$, and $2-3$ are 1417 (1418), 1403 (1408), and 1459 cm^{-1}, respectively, based on the He(I) UPS (VUV−PFI-PE spectrum). The (2 + 1) REMPI spectrum showed the spacings of 1472 and 1442 cm^{-1} for $v_{8a} = 1-0$ and $2-1$. The results may suggest some anharmonicities of the 8a mode. Nevertheless, we have neglected them in the present work. The Duschinsky effect is safely neglected for both the 6a and 8a modes, since the calculated normal modes are quite similar for D_0 and S_0.

Figure 16, panels a and b, presents the relative intensities of the 6a mode in the He(I) photoelectron spectrum and the (2 +

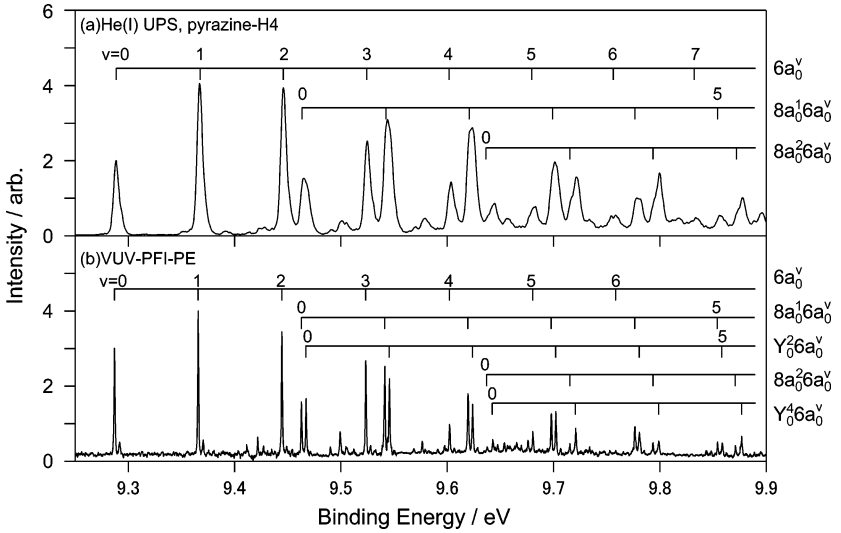

Figure 15. (a) Expanded view of He(I) photoelectron spectrum of pyrazine-H4 with vibrational assignments. (b) VUV-PFI-PE spectra in the $D_0(n^{-1}) \leftarrow S_0$ region.

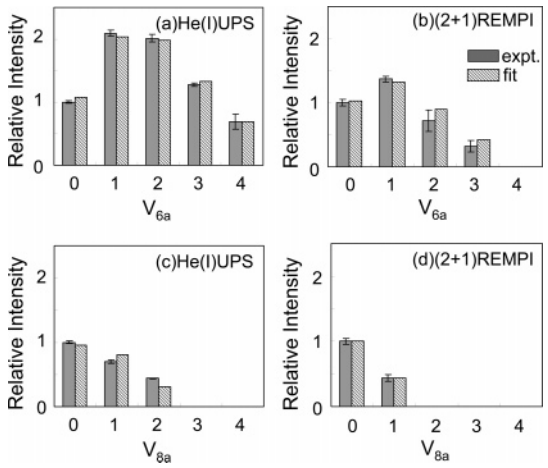

Figure 16. Observed and simulated relative intensities: 6a mode progression in (a) He(I) UPS and (b) (2 + 1) REMPI via $3s(n^{-1})$, and 8a mode progression in (c) He(I) UPS and (d) (2 + 1) REMPI via $3s(n^{-1})$. Relative Intensity was normalized by the intensity of $\upsilon_{6a} = 0$.

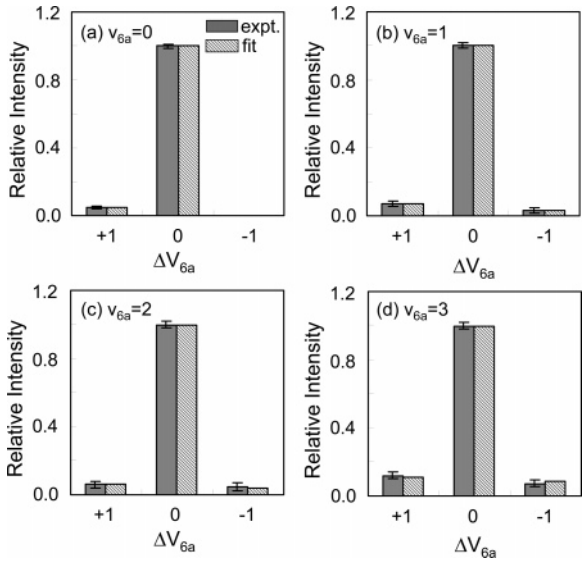

Figure 17. Observed and simulated relative intensities of the 6a mode progression in (2 + 1) photoelectron images via $3s(n^{-1})$ (a) $\upsilon_{6a} = 0$, (b) $\upsilon_{6a} = 1$, (c) $\upsilon_{6a} = 2$, and (d) $\upsilon_{6a} = 3$.

1)REMPI spectrum of pyrazine-H4, respectively, along with the FC fitting. The fitting reproduces experimental relative intensities quite well. The ΔQ_{6a} obtained from the He(I) photoelectron spectrum was 0.462 ± 0.005 in AMU$^{1/2}$ Å unit, and ΔQ_{6a} between the ground state and the $3s(n^{-1})$ state is 0.381 ± 0.009 from the (2 + 1)REMPI spectrum. In the fitting of the 6a mode in the (2 + 1) REMPI spectrum, a weighted least-squares fitting was used. The geometry changes between $D_0(n^{-1})$ and S_0, 0.462 ± 0.005, and the change between the $3s(n^{-1})$ state and S_0, 0.381 ± 0.015, yields the difference between $D_0(n^{-1})$ and the $3s(n^{-1})$ state to be 0.081 ± 0.016. Figure 16, panels c and d, is the relative intensities of the 8a mode. The ΔQ_{8a} obtained from the He(I) photoelectron spectrum and the (2 + 1) REMPI spectrum, which were determined to be 0.190 ± 0.022 and 0.136 ± 0.013, respectively.

Figure 17 presents the relative intensities of the 6a mode in the photoelectron images along with the results of FCF fitting. Panels a−d correspond to the PKEDs obtained in ionization via the $3s(n^{-1}, \upsilon_{6a} = 0-3)$ state of pyrazine-H4, respectively. ΔQ_{6a} between the $D_0(n^{-1})$ and $3s(n^{-1})$ states, 0.060 ± 0.013, is in good agreement with 0.080 ± 0.016 determined from the He(I) photoelectron spectrum and the (2 + 1) REMPI spectrum.

The equilibrium geometry of the upper state in the Cartesian coordinate is given by

$$\mathbf{R}_{eq} = \mathbf{R}'_{eq} + \mathbf{R} \tag{6}$$

where $\mathbf{R}_{eq}$and $\mathbf{R}'_{eq}$ are the equilibrium geometries in the upper state and the ground state in the Cartesian coordinate, respectively, and $\mathbf{R}$ is the change in the equilibrium geometry between these states. The displacement $\Delta\mathbf{Q}$ of the equilibrium geometry between the upper state and the ground state with the normal coordinate is transformed to the Cartesian coordinate as

$$\begin{aligned}\Delta\mathbf{X} &= \mathbf{M}^{-1}(\mathbf{L}^{-1}\mathbf{B})^t\Delta\mathbf{Q} \\ &= \mathbf{l}'_{cart}\mathbf{V}'^{-1/2}\Delta\mathbf{Q}\end{aligned} \tag{7}$$

where $\mathbf{l}'_{cart}$ is the reduced-mass-weighted Cartesian displacement matrix and $\mathbf{V}'$ is the diagonal matrix of reduced masses for each

TABLE 9: Equilibrium Geometries of Pyrazine in D_0 and 3s(n^{-1}) Determined by the He(I) UPS and (2 + 1) REMPSI Spectra

	3s(n^{-1})	D_0
NC/Å	1.315(2)	1.309(2)
CC/Å	1.413(5)	1.424(5)
CH/Å	1.087(1)	1.088(1)
CNC/deg	123.0(4)	124.7(2)
NCC/deg	118.5(2)	117.7(2)
HCN/deg	120.2(5)	121.4(5)

mode in the neutral ground state. Substitution of eq 7 into eq 6 yields

$$\mathbf{R}_{eq} = \mathbf{R}'_{eq} + \mathbf{l}_{cart}\mathbf{V}^{-1/2}\Delta\mathbf{Q} \quad (8)$$

where ΔQ_i is determined by experiments. ΔQ_i's are assumed to be zero except for the 6a and 8a modes. We used calculated values at the B3LYP/cc-pVTZ level for the normal mode $\mathbf{l}'_{cart}$, the reduced mass $\mathbf{V}'$, and the equilibrium geometry $\mathbf{R}'_{eq}$ in the neutral ground state. Since $\mathbf{R}_{eq}$ in eq 8 is in the Cartesian coordinate, $\mathbf{R}_{eq}$ must be transformed to the one in the internal coordinate. The equilibrium geometries in the internal coordinate in D_0 and the 3s Rydberg state are summarized in Table 9. The experimental values slightly differ from the calculated values in the cationic state, which is consistent with the difference between the experimental and calculated spectra discussed above.

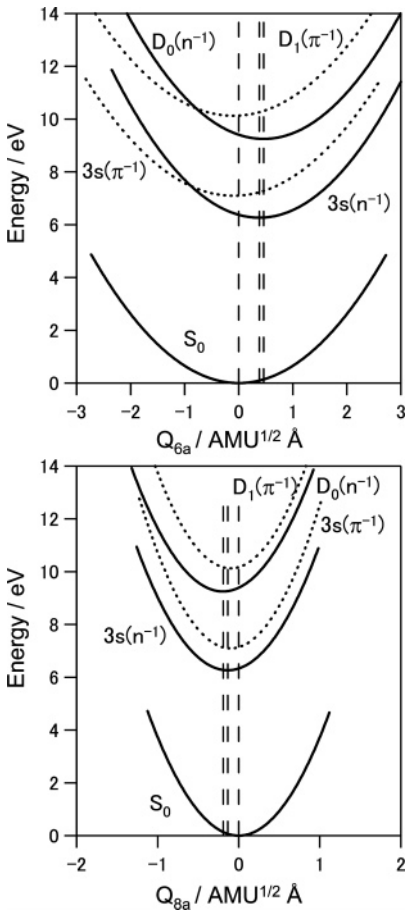

Figure 18. Harmonic potential curves along with 6a and 8a normal coordinate for pyrazine-H4 determined from spectrosispic data. The equilibrium geometries in the 3s(n^{-1}) and D_0(n^{-1}) states changes significantly from the ground state, and the equilibrium geometry in the 3s(n^{-1}) state differs from that in the D_0(n^{-1}) state.

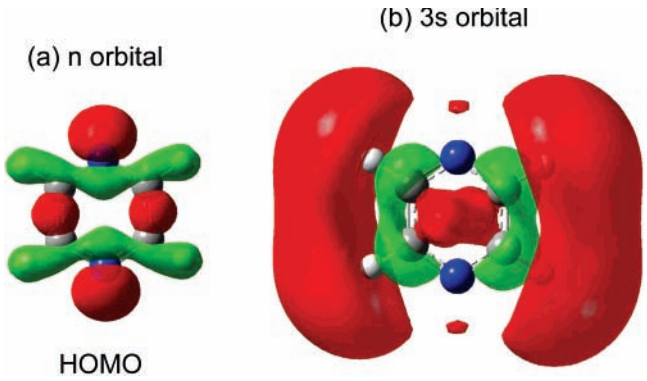

Figure 19. HOMO and the lowest energy orbital of the totally symmetric virtual orbital which corresponds to the 3s orbital at the MP2/aug-cc-pVTZ level of pyrazine. An isovalue of 0.04 au. was used in the GaussView 3.0 program.

IV. Discussion

A. Equilibrium Geometries in $D_0(n^{-1})$ and 3s(n^{-1}). Since the experimentally obtained ΔQ's of $D_0(n^{-1})$ and 3s(n^{-1}) along the 6a and 8a normal coordinates are only absolute values, the signs of these ΔQ's are not readily determined. Therefore, we referred to the calculated equilibrium geometry of $D_0(n^{-1})$ at the B3LYP/cc-pVTZ level and determined their signs. Figure 18 shows the harmonic potential curves along the 6a and 8a normal coordinates, in which the harmonic potential curves of $D_0(n^{-1})$ and 3s(n^{-1}) were obtained in this work, whereas that of $D_1(\pi^{-1})$ was drawn using the ΔQ obtained by Stock and Domcke.[29] We can see conical intersection between the 3s(n^{-1}) and 3s(π^{-1}) and between $D_0(n^{-1})$ and $D_1(\pi^{-1})$.

Figure 19a displays the nonbonding orbital of pyrazine. Although the HOMO is primarily a nonbonding orbital, this orbital is significantly mixed with the σ orbitals of the C−N and C−C bonds due to through-bond interactions between the two nitrogen atoms.[65,66] Structural distortion of the molecule upon removal of an electron from the HOMO is qualitatively understood by considering the σ character that is bonding for C−C and antibonding for C−N. As seen in Table 9, the geometry in 3s(n^{-1}) is intermediate between $D_0(n^{-1})$ and neutral ground state. The geometry difference between $D_0(n^{-1})$ and 3s(n^{-1}) is ascribed to penetration of the 3s Rydberg electron into the ion core. The 3s orbital is considered as a diffuse isotropic orbital at a long distance, yet it has characteristic nodal structures at a short distance, as anticipated from the orthogonality of its eigenfunction with other valence eigenfunctions. Figure 19b shows the lowest virtual orbital of a_g symmetry calculated at the MP2/aug-cc-pVTZ level, that approximately corresponds to the 3s orbital of pyrazine. This orbital has nodes on the C−N bonds, whereas it has a bonding character for the C−C bond. This qualitatively accords with the shorter C−C bond length and the longer C−N bond length in 3s(n^{-1}) than $D_0(n^{-1})$ as listed in Table 9.

B. He(I) UPS and VUV−PFI-PE Spectrum. Although the vibrational feature of the VUV−PFI-PE spectrum is similar to that of the He(I) photoelectron spectrum in the $D_0(n^{-1})$ region, the feature in the $D_1(\pi^{-1})$ region differs dramatically between the two spectra. Only tiny peaks appear in the VUV−PFI-PE spectrum, in which one of the peaks appear at 10.165 71 eV is in reasonably good agreement with the origin band of $D_1(\pi^{-1}) \leftarrow S_0$ determined by the He(I) UPS (10.169(1) eV) (Figure 8).

When an overall intensity distribution in the VUV−PFI-PE $D_1(\pi^{-1})$ band around a strong peak is fit to a single Lorentzian, its fwhm is 25 meV which is considerably smaller than the value

(55 meV) in He(I) UPS. Furthermore, the width of the strongest line is about fwhm of 3.3 meV which is also considerably smaller than the value observed in the He(I) UPS. This spectral feature in the D_1 region in VUV−PFI-PE is not understood yet. Nevertheless, the overall weakness of the D_1 bands is ascribed to short lifetimes of the high-*n* Rydberg states responsible for the VUV−PFI-PE. In our VUV−PFI-PE, field ionization of Rydberg states is induced after a delay time of around hundred nanoseconds to a few microseconds: if the high-*n* Rydberg states autoionize prior to the delay time, they are not observed. It is noted that highly vibrationally excited levels in D_0 do not exhibit anomalies in VUV−PFI-PE, which implies that vibrational autoionization from the vibrationally excited ZEKE states with a D_0 ion core is not fast enough to quench the PFI signals. This also means that vibrationally excited ZEKE states with a D_0 core produced by internal conversion from ZEKE states with a D_1 core are not necessarily short-lived, if there were no additional interaction with the ionization continuum. Thus, we conclude that D_1 ZEKE states electronically autoionize into the D_0 continuum with autoionizing lifetimes shorter than 100 ns.

Similar disappearance of bands in the VUV−PFI-PE spectrum has been observed for the C ($^2\Pi_{1/2u}$) state of the Ar dimer, and it was ascribed to a short lifetime of the high-*n* Rydberg states with the C state as an ion core: the C state dissociates into $Ar(S_0) + Ar^+(^2P_{1/2})$.[67] In the VUV−PFI-PE study of NO_2, the b($^3A_2$) band was observed much more weakly than that observed in the He(I) UPS.[68,69] However, the present result on pyrazine is perhaps the clearest example of the significant difference between VUV−PFI-PE and UPS in observation of ionic states with short lifetimes. We note that in addition to fast autoionization processes, fast neutral dissociation and fluorescence processes of excited species in high-*n* Rydberg states can also lead to weakening or disappearance of the PFI-PE signal.

C. Implication to S_2-S_1 Conical Intersection. The S_2-S_1 internal conversion in pyrazine is a benchmark system for the study of nonadiabatic dynamics through a conical intersection in polyatomic molecules.[26,28−30,32] The S_1 and S_2 potential energy surfaces of this molecule have been obtained by ab initio MO calculations,[27] and the topographical features of the conical intersection have been elucidated. A special feature of this conical intersection, which is common with the D_1-D_0 case, is that only the mode 10a(b_{1g}) induces the avoided crossing between the two states. It has been shown by calculations, including the exact treatment of nuclear motions, the path integral,[31] and the multiconfiguration time-dependent Hartree (MCTDH) methods,[32] that the short-time nuclear dynamics occurs along four totally symmetric modes and the mode 10a, whereas weaker vibrational couplings with other modes contribute to long-time behaviors. Due to computational loads, accurate dynamical calculations are only possible for several vibrational modes, and other modes are often treated phenomenologically or semiquantitatively. Since dynamical calculations in reduced dimensions tend to provide considerably narrower line-widths for the $S_2 \leftarrow S_0$ spectrum than the experimental ones, the effects of weak couplings of many vibrational modes are usually adjusted so as to reproduce the experimental linewidths.

Although previous He(I) spectrum of pyrazine vapor exhibited a very broad feature in the D_1 region,[24] our He(I) UPS of jet-cooled pyrazine resolved finer vibrational structures. Since the D_1-D_0 conical intersection resembles the S_2-S_1 case, the result suggests that the S_2-S_0 absorption spectrum of jet-cooled pyrazine may exhibit more distinct features than the one observed using a thermal pyrazine sample at room temperature. The experimental spectrum referred by all of the theoretical studies on S_2-S_1 internal conversion so far was the absorption spectrum of pyrazine vapor at room temperature reported by Yamazaki et al.,[11] and it seems necessary to measure the S_2-S_0 absorption spectrum of jet-cooled pyrazine to allow a closer comparison with the theoretical simulation using state-of-the-art techniques for multidimensional nonadiabatic nuclear dynamics.

D. Formation of Fragment Ions. We observed fragment masses in nanosecond REMPI via 3s(n^{-1}) and 3s(π^{-1}) and picosecond REMPI via 3s(π^{-1}), which indicates that internal conversion processes occur from these Rydberg states to lower valence electronic states, leading to either fragmentation in these states or formation of highly vibrationally excited states (hot molecules). If dissociation occurs in the neutral valence states, the fragment ions are formed by ionization of these neutral fragments, whereas multiphoton ionization of hot pyrazine will also result in fragmentation in the cationic state to produce daughter ions. The similar lifetimes estimated from homogeneous line-broadening of 3s(π^{-1}) and $D_1(\pi^{-1})$ indicates that the primary deactivation path from 3s(π^{-1}) is to 3s(n^{-1}). This is essentially a relaxation in the ion core of the Rydberg state. Homogeneous line-broadening of the 3s(n^{-1}) band also indicates that this state undergoes internal conversion to excited valence states and/or the ground electronic states within 300 fs. Thus, within 300 fs the system should result in formation of valence states. Other evidence indicates that S_2 and S_1 are also short-lived: Yamasaki et al. have observed the fluorescence lifetimes of S_1 vibronic states for pyrazine vapor and observed 25 ps near the S_2 origin,[11] and TRPEI by Wang et al. have observed 22 and 39 ps for pyrazine-H4 and D4 following 264 nm excitation to the S_2 origin which are regarded as the lifetimes of hot S_1 pyrazine after ultrafast S_2-S_1 internal conversion.[2] The lifetime of S_2 state is estimated to be less than 30 fs due to $S_2 \rightarrow S_1$ internal conversion.

The rovibronic energy of pyrazine given by photoexcitation to the 3s manifold is as large as 145−170 kcal/mol, whereas the barriers for dissociation in S_0 are smaller than these values.[70,71] Therefore, if internal conversion occurs to S_0, they undergo dissociation. However, dissociation dynamics in the ground state is generally in a microsecond time scale: Ni and co-workers have studied photodissociation of pyrimidine and pyridine after 193 and 248 nm photoexcitation, in which they found dissociation rate of the order of 10^6/s except for 193 nm photodissociation of pyridine.[71] Therefore, it is likely that nanosecond REMPI experiment is ionizing hot pyrazine molecule prior to their unimolecular decay on the S_0 surface, and the subsequent dissociation of internally excited cation produces the daughter ions. In this scenario, the difference of the yields of fragment masses between nanosecond and picosecond REMPI is explained rather well, although a possibility of fast dissociation on the valence state of pyrazine cannot be completely ruled out without further investigation. One of the ways to examine dissociation dynamics is to observe recoil velocity distributions of fragment ions: if rapid dissociation takes place in excited electronic states of pyrazine, it is likely that the photofragments exhibit anisotropic distributions and translational energy release peaking at certain energy.[55] It would also be helpful to perform pump and probe experiment to directly measure the reaction rate for understanding the origin of the fragment masses. Nanosecond (2 + 1) REMPI of pyrimidine via the 3p Rydberg state also produces fragment masses at $m/e = 26$ and 53,

similarly with the pyrazine case.[72] Therefore, the formation mechanism of the daughter ions from pyrazine and pyrimidine may be similar to each other.

V. Conclusions

We have studied molecular structures of pyrazine in the 3s Rydberg states and the ground and excited states of its cation. Several photoelectron spectroscopic methods, including the UPS, the VUV-PFI-PE and the photoelectron imaging detection schemes, were used to investigate structural differences between the S_0, 3s, and D_0 states. These states were interpreted in terms of characters of an ionized nonbonding orbital and a singly occupied 3s Rydberg orbital. Internal conversion dynamics from D_1 to D_0 was studied in the frequency domain, and the lifetime of an optically bright state and the characters of the doorway states were elucidated. It is suggested that internal conversion rate from D_1 to D_0 is faster in pyrazine-H4 whereas vibrational dephasing from the doorway states to background bath states may be faster in pyrazine-D4. It would be of interest to compare the observed spectroscopic features of the doorway states with theoretical calculations. Missing feature of D_1 in the VUV-PFI-PE measurement is ascribed to fast electronic autoionization from high-*n* Rydberg (ZEKE) states to the D_0 continuum. This work demonstrates that the high-resolution attainable by VUV-PFI-PE measurements and the versatility of UPS offer complementary information on the ionic states, and a combined study offers more insights into the dynamics in ionic states and high-*n* Rydberg states.

Acknowledgment. We gratefully acknowledge Dr. Atsushi Iwasaki for his experimental assistance. This work was supported by Grant-in-Aid from the Ministry of Education, Culture, Sports, Science and Technology (17205004). C.Y.N. acknowledges the support by the DOE Contract No. DE-FG02-02ER15306, the AFOSR Grant No. FA9550-06-1-0073, and the NSF Grant No. CHE-0517871.

References and Notes

(1) Suzuki, T. *Annu. Rev. Phys. Chem.* **2006**, *57*, 555.
(2) Wang, L.; Kohguchi, H.; Suzuki, T. *Faraday Discuss* **1999**, *113*, 37.
(3) Frad, A.; Lahmani, F.; Tramer, A.; Tric, C. *J. Chem. Phys.* **1974**, *60*, 4419.
(4) Lahmani, F.; Tramer, A.; Tric, C. *J. Chem. Phys.* **1974**, *60*, 4431.
(5) Avouris, P.; Gelbart, W. M.; El-Sayed, M. A. *Chem. Rev.* **1977**, *77*, 793.
(6) McDonald, D. B.; Fleming, G. R.; Rice, S. A. *Chem. Phys.* **1981**, *60*, 335.
(7) Bixon, M.; Jortner, J. *J. Chem. Phys.* **1968**, *48*, 715.
(8) Felker, P. M.; Lambert, W. R.; Zewail, A. H. *Chem. Phys. Lett.* **1982**, *89*, 309.
(9) Saigusa, H.; Lim, E. C. *Chem. Phys. Lett.* **1982**, *88*, 455.
(10) Matsumoto, Y.; Spangler, L. H.; Pratt, D. W. *Chem. Phys. Lett.* **1983**, *98*, 333.
(11) Yamazaki, I.; Murao, T.; Yamanaka, T.; Yoshihara, K. *Faraday Discuss* **1983**, *75*, 395.
(12) Knee, J. L.; Doany, F. E.; Zewail, A. H. *J. Chem. Phys.* **1985**, *82*, 1042.
(13) Lorincz, A.; Smith, D. D.; Novak, F.; Kosloff, R.; Tannor, D. J.; Rice, S. A. *J. Chem. Phys.* **1985**, *82*, 1067.
(14) Kommandeur, J.; Majewski, W. A.; Meerts, W. L.; Pratt, D. W. *Annu. Rev. Phys. Chem.* **1987**, *38*, 433.
(15) Felker, P. M.; Zewail, A. H. *Chem. Phys. Lett.* **1986**, *128*, 221.
(16) Tsubouchi, M.; Whitaker, B. J.; Wang, L.; Kohguchi, H.; Suzuki, T. *Phys. Rev. Lett.* **2001**, *86*, 4500.
(17) Suzuki, T.; Wang, L.; Tsubouchi, M. *J. Phys. Chem. A* **2004**, *108*, 5764.
(18) Tsubouchi, M.; Whitaker, B. J.; Suzuki, T. *J. Phys. Chem. A* **2004**, *108*, 6823.
(19) Suzuki, T.; Whitaker, B. J. *Int. Rev. Phys. Chem.* **2001**, *20*, 313.
(20) Song, J. K.; Tsubouchi, M.; Suzuki, T. *J. Chem. Phys.* **2001**, *115*, 8810.
(21) Turner, R. E.; Vaida, V.; Molini, C. A.; Berg, J. O.; Parker, D. H. *Chem. Phys.* **1978**, *28*, 47.
(22) Dion, C. F.; Bernstein, E. R. *J. Chem. Phys.* **1995**, *103*, 4907.
(23) Åsbrink, L.; Lindholm, E.; Edqvist, O. *Chem. Phys. Lett.* **1970**, *5*, 609.
(24) Fridh, C.; Åsbrink, L.; Jonsson, B.; Lindholm, E. *Int. J. Mass. Spec. Ion Phys.* **1972**, *8*, 101.
(25) Seidner, L.; Domcke, W.; von Niessen, W. *Chem. Phys. Lett.* **1993**, *205*, 117.
(26) Stock, G.; Schneider, R.; Domcke, W. *J. Chem. Phys.* **1989**, *90*, 7184.
(27) Schneider, R.; Domcke, W.; Köppel, H. *J. Chem. Phys.* **1990**, *92*, 1045.
(28) Seel, M.; Domcke, W. *J. Chem. Phys.* **1991**, *95*, 7806.
(29) Stock, G.; Domcke, W. *J. Phys. Chem.* **1993**, *97*, 12466.
(30) Woywod, C.; Domcke, W.; Sobolewski, A. L.; Werner, H. J. *J. Chem. Phys.* **1994**, *100*, 1400.
(31) Krempl, S.; Winterstetter, M.; Domcke, W. *J. Chem. Phys.* **1995**, *102*, 6499.
(32) Raab, A.; Worth, G. A.; Meyer, H.-D.; Cederbaum, L. S. *J. Chem. Phys.* **1999**, *110*, 936.
(33) Müller-Dethlefs, K.; Sander, M.; Schlag, E. W. *Chem. Phys. Lett.* **1984**, *112*, 291.
(34) Müller-Dethlefs, K.; Sander, M.; Schlag, E. W. *Z. Naturforsch. A* **1984**, *39*, 1089.
(35) Müller-Dethlefs, K.; Dopfer, O.; Wright, T. G. *Chem. Rev.* **1994**, *94*, 1845.
(36) Schlag, E. W. *Zeke Spectroscopy*; Cambridge University Press: Cambridge, 1998.
(37) Ng, C. Y. *Annu. Rev. Phys. Chem.* **2002**, *53*, 101.
(38) Woo, H. K.; Zhan, J.; Lau, K.-C.; Ng, C. Y.; Cheung, Y.-S. *J. Chem. Phys.* **2002**, *116*, 8803.
(39) Woo, H. K.; Wang, P.; Lau, K. C.; Xing, X.; Ng, C. Y. *J. Phys. Chem. A* **2004**, *108*, 9637.
(40) Zhu, L.; Johnson, P. *J. Chem. Phys.* **1993**, *99*, 2322.
(41) Wrede, E.; Laubach, S.; Schulenburg, S.; Brown, A.; Wouters, E. R.; Orr-Ewing, A. J.; Ashfold, M. N. R. *J. Chem. Phys.* **2001**, *114*, 2629.
(42) Ohrwall, G.; Baltzer, P.; Bozek, J. *Phys. Rev. A* **1999**, *59*, 1903.
(43) Frisch, M. J.; Trucks, G. W.; Schlegel, H. B.; Scuseria, G. E.; Robb, M. A.; Cheeseman, J. R.; Montgomery, J. A., Jr.; Vreven, T.; Kudin, K. N.; Burant, J. C.; Millam, J. M.; Iyengar, S. S.; Tomasi, J.; Barone, V.; Mennucci, B.; Cossi, M.; Scalmani, G.; Rega, N.; Petersson, G. A.; Nakatsuji, H.; Hada, M.; Ehara, M.; Toyota, K.; Fukuda, R.; Hasegawa, J.; Ishida, M.; Nakajima, T.; Honda, Y.; Kitao, O.; Nakai, H.; Klene, M.; Li, X.; Knox, J. E.; Hratchian, H. P.; Cross, J. B.; Bakken, V.; Adamo, C.; Jaramillo, J.; Gomperts, R.; Stratmann, R. E.; Yazyev, O.; Austin, A. J.; Cammi, R.; Pomelli, C.; Ochterski, J. W.; Ayala, P. Y.; Morokuma, K.; Voth, G. A.; Salvador, P.; Dannenberg, J. J.; Zakrzewski, V. G.; Dapprich, S.; Daniels, A. D.; Strain, M. C.; Farkas, O.; Malick, D. K.; Rabuck, A. D.; Raghavachari, K.; Foresman, J. B.; Ortiz, J. V.; Cui, Q.; Baboul, A. G.; Clifford, S.; Cioslowski, J.; Stefanov, B. B.; Liu, G.; Liashenko, A.; Piskorz, P.; Komaromi, I.; Martin, R. L.; Fox, D. J.; Keith, T.; Al-Laham, M. A.; Peng, C. Y.; Nanayakkara, A.; Challacombe, M.; Gill, P. M. W.; Johnson, B.; Chen, W.; Wong, M. W.; Gonzalez, C.; Pople, J. A. *Gaussian 03*; Gaussian, Inc.: Wallingford, CT, 2004.
(44) Werner, H.-J.; Knowles, P. J.; Lindh, R.; Manby, F. R.; Sch′z, M.; Celani, P.; Korona, T.; Rauhut, G.; Amos, R. D.; Bernhardsson, A.; Berning, A.; Cooper, D. L.; Deegan, M. J. O.; Dobbyn, A. J.; Eckert, F.; Hampel, C.; Hetzer, G.; Lloyd, A. W.; McNicholas, S. J.; Meyer, W.; Mura, M. E.; Nicklass, A.; Palmieri, P.; Pitzer, R.; Schumann, U.; Stoll, H.; Stone, A. J.; Tarroni, R.; Thorsteinsson, T. *MOLPRO*.
(45) Innes, K. K.; Byrne, J. P.; Ross, I. G. *J. Mol. Spectrosc.* **1967**, *22*, 125.
(46) Cradock, S.; Liescheski, P. B.; Rankin, D. W. H.; Robertson, H. E. *J. Am. Chem. Soc.* **1988**, *110*, 2758.
(47) Bormans, M.; With, G. D.; Mijlhoff, F. C. *J. Mol. Struct.* **1977**, *42*, 121.
(48) Martin, J. M. L.; Van Alsenoy, C. *J. Phys. Chem* **1996**, *100*, 6973.
(49) Innes, K. K.; Ross, I. G.; Moomaw, W. R. *J. Mol. Spectrosc.* **1988**, *132*, 492.
(50) Goto, A.; Fujii, M.; Ito, M. *Chem. Phys. Lett.* **1987**, *135*, 407.
(51) Mulliken, R. S. *J. Chem. Phys.* **1955**, *23*, 1997.
(52) Udagawa, Y.; Ito, M.; Suzuka, I. *Chem. Phys.* **1980**, *46*, 237.
(53) Parkin, J. E.; Innes, K. K. *J. Mol. Spectrosc.* **1965**, *15*, 407.
(54) Yoshino, K.; Freeman, D. E. *J. Opt. Soc. Am. B* **1985**, *2*, 1268.
(55) Shibata, T.; Suzuki, T. *Chem. Phys. Lett.* **1996**, *262*, 115.
(56) Goto, A.; Fujii, M.; Ito, M. *J. Phys. Chem.* **1987**, *91*, 2268.

(57) Baltzer, P.; Karlsson, L.; Wannberg, B.; Öhrwall, G.; Holland, D. M. P.; MacDonald, M. A.; Hayes, M. A.; Van Niessen, W. *Chem. Phys.* **1997**, *224*, 95.
(58) Chen, P. Photoelectron spectroscopy of relative intermediates. In *Unimolecular and Bimolecular Reaction Dynamics*; Ng, C. Y., Bear, T., Powis, I., Eds.; Wiley: New York, 1994; pp 371.
(59) Kohn, D. W.; Robles, E. S. J.; Logan, C. F.; Chen, P. *J. Phys. Chem* **1993**, *97*, 4936.
(60) Kohn, D. W.; Chen, P. *J. Am. Chem. Soc.* **1993**, *115*, 2844.
(61) Luis, J. M.; Bishop, D. M.; Kirtman, B. *J. Chem. Phys.* **2004**, *120*, 813.
(62) Sharp, T. E.; Rosenstock, H. M. *J. Chem. Phys.* **1964**, *41*, 3453.
(63) Hutchisson, E. *Phys. Rev.* **1930**, *36*, 410.
(64) Duschinsky, F. *Acta Physicochim. U.R.S.S.* **1937**, *11*, 551.
(65) Gleiter, R.; Hornung, V.; Heilbron, E. *Helv. Chem. Acta.* **1972**, *55*, 255.
(66) Hoffmann, R. *Acc. Chem. Res.* **1971**, *4*, 1.
(67) Onuma, T.; Yoshii, H.; Ishijima, H.; Itou, Y.; Hayaishi, T.; Morioka, Y. *J. Mol. Spectrosc.* **1999**, *198*, 209.
(68) Jarvis, G. K.; Song, Y.; Ng, C. Y.; Grant, E. R. *J. Chem. Phys.* **1999**, *111*, 9568.
(69) Kimura, K.; Katsumata, S.; Achica, Y.; Yamazaki, T.; Iwata, S. *Handbook of HeI Photoelectron Spectra of Fundamental Organic Molecules*; Japan Scientific Societies: Tokyo, 1981.
(70) Lin, M.-F.; Dyakov, Y. A.; Tseng, C.-M.; Mebel, A. M.; Lin, S. H.; Lee, Y. T.; Ni, C.-K. *J. Chem. Phys.* **2005**, *123*, 054309.
(71) Lin, M.-F.; Dyakov, Y. A.; Tseng, C.-M.; Mebel, A. M.; Lin, S. H.; Lee, Y. T.; Ni, C.-K. *J. Chem. Phys.* **2006**, *124*, 084303.
(72) Philis, J. G. *J. Mol. Spectrosc.* **2005**, *232*, 26.